Structural variability, coordination, and adaptation of a native photosynthetic machinery

Long-Sheng Zhao[1,2,3,4], Tuomas Huokko[2], Sam Wilson[5], Deborah M. Simpson[2], Qiang Wang[6], Alexander V. Ruban[5], Conrad W. Mullineaux[5], Yu-Zhong Zhang[1,3,4,*], Lu-Ning Liu[2,3,*]

[1] State Key Laboratory of Microbial Technology, and Marine Biotechnology Research Center, Shandong University, Qingdao 266237, China.

[2] Institute of Integrative Biology, University of Liverpool, Liverpool L69 7ZB, United Kingdom

[3] College of Marine Life Sciences, and Frontiers Science Center for Deep Ocean Multispheres and Earth System, Ocean University of China, Qingdao 266003, China

[4] Laboratory for Marine Biology and Biotechnology, Pilot National Laboratory for Marine Science and Technology, Qingdao 266237, China

[5] School of Biological and Chemical Sciences, Queen Mary University of London, Mile End Road, London E1 4NS, United Kingdom

[6] State Key Laboratory of Crop Stress Adaptation and Improvement, School of Life Sciences, Henan University, Kaifeng 475004, China

*Corresponding authors: luning.liu@liverpool.ac.uk (L.-N.L.), zhangyz@sdu.edu.cn (Y.-Z.Z.)

Abstract

Cyanobacterial thylakoid membranes represent the active sites for both photosynthetic and respiratory electron transport. We used high-resolution atomic force microscopy to visualise the native organisation and interactions of photosynthetic complexes within the thylakoid membranes from the model cyanobacterium *Synechococcus elongatus* PCC 7942. The thylakoid membranes are heterogeneous and assemble photosynthetic complexes into functional domains to enhance their coordination and regulation. Under high light, the chlorophyll-binding proteins IsiA are strongly expressed and associates with Photosystem I (PSI) forming highly variable IsiA−PSI supercomplexes to increase the absorption cross-section of PSI. There are also tight interactions of PSI with Photosystem II (PSII), cytochrome b_6f, ATP synthase, and NAD(P)H dehydrogenase complexes. The organisational variability of these photosynthetic supercomplexes permits efficient linear and cyclic electron transport and bioenergetic regulation. Understanding the organisational landscape and environmental adaptation of cyanobacterial thylakoid membranes may help inform strategies for engineering efficient photosynthetic systems and photo-biofactories.

Introduction

Phototrophic prokaryotes have evolved intracytoplasmic membranes to maximise photosynthetic light absorption and fulfil energy transduction. A superior example of bacterial intracytoplasmic membranes is the thylakoid membrane found in most cyanobacteria[1], which represents one of the most important and complicated membrane systems in nature[2,3].

The cyanobacterial thylakoid membrane is densely packed by various membrane protein complexes that are responsible for both photosynthetic and respiratory electron transport[1]. Photosynthetic electron transport is carried out mainly by four membrane-spanning macromolecular complexes, photosystems I (PSI), photosystems II (PSII), cytochrome b_6f complex (Cyt b_6f) and ATP synthase (ATPase), homologous to the photosynthetic complexes in chloroplasts. The main light-harvesting antenna for PSII in cyanobacteria is the phycobilisome, a large pigment-binding macromolecular complex associated with the thylakoid membrane[1,4]. There is also a membrane-spanning protein associated with PSI, known as IsiA, which is expressed under stress conditions[5-10]. However, the role of IsiA is still unclear. It has been proposed to function as an accessory antenna for PSI. Recent electron microscopy revealed that each IsiA monomer coordinates 17 chlorophyll (Chl) molecules and 18 IsiA can encircle a PSI trimer to form an IsiA−PSI supercomplex[11,12]. Thus, the IsiA−PSI supercomplex exhibits an 81% increase of optical cross-section and enhanced energy transfer compared to PSI trimer alone[13,14]. PSI can also be surrounded by two IsiA rings, 18 IsiA monomers in the first ring and 25 in the second ring, forming a larger IsiA−PSI supercomplex[15]. Other proposed roles of IsiA are an energy dissipator for photoprotection[9,16] and Chl storage[17]. Additionally, cyanobacterial thylakoid membranes also accommodate components of the respiratory electron transport chains, comprising type-I NAD(P)H dehydrogenase (NDH-1), succinate dehydrogenase, and terminal oxidases[2,3]. The intricate organisation, functional links, and regulation of different electron transport complexes in the thylakoid membrane are critical for cyanobacterial bioenergetics and growth in varying ecophysiological environments.

Despite substantial information about the structures and functions of individual bioenergetic complexes, our knowledge about how these electron transport complexes are organised and physiologically coordinated with others in native thylakoid membranes remains primitive. The cyanobacterial thylakoid membrane network is laterally heterogeneous, resembling plant chloroplast and mitochondrial membranes[18]. Using fluorescent tagging, recent studies have demonstrated the heterogeneous distribution of photosynthetic complexes in thylakoid membranes from the model cyanobacterium *Synechococcus elongatus* PCC 7942

65 (Syn7942)[19] and the lateral segregation of PSI in *Synechocystis* sp. PCC 6803 (Syn6803)[20]. The complexity

66 of cyanobacterial thylakoid membranes features the formation of photosynthetic megacomplexes to facilitate

67 defined electron transfer pathways[21,22].

68   Atomic force microscopy (AFM) has become a unique and powerful tool in studying membrane

69 protein structure, organisation, and dynamics in photosynthetic membranes at the near-physiological

70 context[23]. AFM possesses a high signal-to-noise ratio, thus with no requirement for data averaging, and

71 permits direct visualisation of membrane proteins in the native environment in solution, avoiding complex

72 purification and detergent treatment. Medium-resolution AFM images have revealed the PSI organisation

73 and intermixture of PSI, PSII, and Cyt b_6f complexes in the thylakoid membranes from various

74 cyanobacterial species[19,20,24]. However, the lateral associations and structural adaptation of the electron

75 transport supercomplexes in cyanobacterial thylakoid membranes are still missing.

76   Here, we apply high-resolution AFM imaging to draw a landscape view of the native arrangement of

77 membrane complexes in the thylakoid membrane from Syn7942. Our results provide novel insight into the

78 heterogeneity, compartmentalisation and functional regulation of cyanobacterial photosynthetic apparatus,

79 which is extendable to other membrane systems in bacteria, chloroplasts, and mitochondria. The naturally

80 occurring organisational features of thylakoid membranes could be important considerations for the future

81 engineering of artificial photosynthetic systems to underpin biofuel production.

82

83 **High light induces IsiA expression and formation of the IsiA−PSI supercomplex**

84 The transcription of the IsiA-encoding gene (*isiA*) is regulated by two transcription factors, RpaB (regulator

85 of phycobilisome association B) and Fur (Ferric Uptake Regulator)[25]. RpaB controls the transcription of

86 photosynthesis-associated genes in response to light[25]. Its binding motif, a high-light regulatory (HLR)

87 sequence, is at upstream of many high-light-inducible genes including *isiA* (Supplementary Fig. 1a)[25,26]. Fur

88 is could repress *isiA* expression under iron-replete condition, by binding the Fur box region of *isiA*

89 (Supplementary Fig. 1a)[8]. These facts suggest that the expression of *isiA* could be regulated by both iron

90 availability and light intensity.

91   The thylakoid membranes were isolated from the wild-type (WT) Syn7942 cells grown under

92 moderate light (ML, 40 μmol photons m^{-2} s^{-1})[27-29], high light (HL, 300 μmol photons m^{-2} s^{-1}), or iron

93 deficiency (Fe-), using low ion-concentration buffers in the absence of any detergents. This allowed us to

94 obtain large thylakoid membranes with the size of up to 1 μm[19], which are mostly free of phycobilisomes

95 (disassociated from the thylakoid membrane and disassembled in low ion-concentration buffers), ideal for

96 the long-range membrane organisation imaging by AFM. Absorption spectra (Supplementary Fig. 1), mass

97 spectrometry, and sodium dodecyl sulfate polyacrylamide gel electrophoresis (SDS-PAGE) combined with

98 immunoblot analyses (Supplementary Fig. 2) confirmed that both HL and iron-deficiency treatments could

99 induce IsiA expression, leading to the elevated IsiA content in Syn7942 thylakoids. The IsiA amount in the

100 Fe- adapted thylakoid membranes was about 4.5-fold higher than that in the HL-adapted membranes

101 (Supplementary Fig. 2a). By contrast, the PSI content relative to the total thylakoid protein content in

102 thylakoid membranes was reduced under both HL and iron deficiency (Supplementary Fig. 2a, 2b). These

103 changes led to an increased IsiA:PSI ratio in the HL- and Fe- thylakoid membranes. Blue native

104 polyacrylamide gel electrophoresis (BN-PAGE) and immunoblot analysis further indicated that IsiA could

105 bind with PSI to form IsiA−PSI complexes (Supplementary Fig. 2d, 2e). The PSII and Cyt b_6f content was

106 decreased under HL, similar to PSI, but was slightly increased under Fe- compared to ML (Supplementary

107 Fig. 2a). The PSII dimer:monomer ratio was relatively similar between Fe- and ML conditions and was

108 reduced under HL (Supplementary Fig. 2f). The amount of ATPase was constant under ML and HL

109 (Supplementary Fig. 2a, 2c) and was elevated under Fe- compared to that under ML (Supplementary Fig. 2a).

110 We performed high-resolution AFM imaging on the isolated thylakoid membranes to dissect the

111 native structures and membrane organisation of bioenergetic supercomplexes. AFM topographs showed that

112 membrane proteins were densely packed in both ML- and HL-adapted thylakoid membranes (Fig. 1a, 1b, 1e,

113 1f). ML-adapted thylakoid membrane contains predominately the trimeric structures (triangles), as well as

114 some dimeric (oval) and monomeric features (square) (Fig. 1c). The trimeric structure has the protruding

115 height of 2.58 ± 0.16 nm ($n = 30$) above membrane surface and possesses a three-fold rotational symmetry,

116 with the angle between the long axes of the three protrusions of approximately 120°, consistent with the

117 characteristic cytoplasmic-side structure (referring to PsaC, PsaD, and PsaE subunits) of cyanobacterial PSI

118 trimers (Fig. 1d)[19,30]. Thus, these trimeric structures were assigned to be PSI trimers. PSI trimers have no

119 specific orientation and coexist with PSI dimers and monomers in the Syn7942 thylakoid membranes (Fig.

120 1c). Diverse arrangement patterns of PSI trimers were identified in the ML-adapted thylakoid membranes

121 (Supplementary Fig. 3), indicative of the aggregation flexibility of PSI complexes. This may provide a

122 means for adjusting PSI contents per membrane area to regulate photosynthetic electron transport.

123   Compared to the ML-adapted thylakoid membranes, HL results in the reduction of the PSI content

124   (69%) and the proportion of PSI trimers in the total PSI in the HL-adapted membranes (Supplementary Table

125   1). PSI complexes (circles) were less densely distributed in the HL-adapted thylakoid membranes and were

126   laterally separated from their neighbouring PSI by proteins that are remarkably smaller than PSI monomers

127   (Fig. 1e, 1f, 1g, Supplementary Table 1). These proteins form ring-like or arc structures around PSI to

128   construct PSI-centred supramolecular assemblies (Fig. 1g), resembling the IsiA−PSI complexes from iron-

129   limited cyanobacteria (Fig. 1h)[6,7,11,12]. The overall height of IsiA proteins is 4.3 ± 0.1 nm ($n = 5$), less than

130   that of PSI without PsaC, PsaD, and PsaE (5.0 ± 0.1 nm, $n = 15$) (Supplementary Fig. 4). These results

131   revealed that HL, which has notable impacts on the organisations of thylakoid membrane complexes and

132   CO_2-fixing organelles of Syn7942[19,27-29], could induce the biosynthesis of IsiA to become the major proteins

133   in cyanobacterial thylakoid membranes and form IsiA−PSI supercomplexes.

134   In addition, some structures with an ordered organisation (Fig. 1a, white arrows) and ring structures

135   (Fig. 1c, 1g, blue arrows) were tentatively identified as PSII and ATPase complexes, respectively (see

136   detailed analysis below).

137

138   **Nanodissection of PSI subunits**

139   Continuous AFM imaging on the same membrane with gentle scanning force (< 100 picoNewton) resulted in

140   the removal of strongly-protruded PsaC, PsaD, and PsaE subunits from intact PSI (Fig. 2a, 2b), indicative of

141   their weak interactions with the PSI base at the cytoplasmic side. Figs. 2c and 2d display the representative

142   images of the PSI trimers before and after the PSI protrusions were dissected by the AFM probe (arrows).

143   The distance between two protrusions within the PSI trimer is 10.3 ± 1.0 nm (Fig. 2e, 2f), consistent with

144   that determined from the crystal structure of PSI trimers (11 nm, PDB: 1JB0)[30] (Fig. 2g). The height of the

145   protrusion structures is 2.0 ± 0.3 nm, in agreement with the heights of PsaC, PsaD, and PsaE subunits (2.6

146   nm) (Fig. 2g). Removal of PsaC, PsaD, and PsaE permitted visualisation of the fine surface textures of PSI

147   underneath these subunits in great details (Fig. 2h). Three "ridges" on the surface of each monomer were

148   discerned, in line with the cytoplasmic structure of PSI monomers without PsaC, PsaD, and PsaE (Fig. 2i),

149   further confirming that these strongly protruded features were PSI complexes.

150

151   **Distribution and structural heterogeneity of IsiA−PSI supercomplexes in thylakoid membranes**

152 AFM topographs showed that a typical IsiA−PSI trimer complex possesses a round structure with three-fold

153 rotational symmetry (Fig. 3a); eighteen IsiA monomers form a ring encompassing the PSI trimer, in close

154 agreement with the cryo-electron microscopy (cryo-EM) structure of IsiA−PSI trimers (PDB: 6NWA)[11] and

155 the simulated AFM image based on the cryo-EM structure (Fig. 3a). Contrary to the homogeneous structure

156 obtained from averaged EM images[6,7,11,12,15,31], AFM images revealed the inherent structural variability of

157 IsiA−PSI supercomplexes in native thylakoid membranes (Fig. 3b-3f, Supplementary Figs. 5, 6). PSI trimers,

158 dimers, and monomers can be encircled by IsiA single, double, triple, or multimeric rings, respectively,

159 forming diverse IsiA−PSI structures varying in dimension (Fig. 3b, Supplementary Fig. 5). Approximately

160 71% of the IsiA−PSI supercomplexes possessed one IsiA ring and as the number of rings increased the

161 content of corresponding supercomplexes decreased gradually (Supplementary Table 2). The distribution and

162 orientation of diverse IsiA−PSI supercomplexes were readily random (Fig. 3c-3f, Supplementary Fig. 6).

163   The first closed IsiA ring associated with PSI commonly consists of 18 peaks of IsiA monomers (Fig.

164 4a), consistent with the EM results[6,7,11,12,15] (Fig. 1h). The average distance between adjacent IsiA protrusions

165 in the first ring enclosing the PSI trimer is 4.5 ± 0.1 nm ($n = 160$), larger than those within the second ($4.2 \pm$

166 0.1 nm, $n = 91$), the third (4.2 ± 0.2 nm, $n = 17$), the fourth rings (4.2 ± 0.1 nm, $n = 5$), and IsiA-only

167 assemblies (4.2 ± 0.1 nm, $n = 104$) (Fig. 4a, 4b, 4c). Regardless of the oligomeric states of PSI, the IsiA

168 intervals within the second, third or fourth ring, as well as in the IsiA-only assemblies are similar, but in all

169 above it is less than that in the first ring that directly contacts PSI (Two-sided two-sample t-Test, $p < 0.001$)

170 (Fig. 4c). These results suggested that the binding between IsiA and PSI can modify the lateral arrangement

171 of IsiA in the membrane. The smaller space between adjacent IsiA at the peripheral rings may facilitate

172 excitation energy transfer between Chls of neighbouring IsiA proteins within the same ring, whereas the

173 larger space between adjacent IsiA in the first ring that directly contacts PSI may weaken energy transfer

174 between IsiA subunits and favour energy transfer towards the central PSI. In addition, the first IsiA rings are

175 often intact, whereas complete IsiA circles were barely seen in the following rings as well as the first ring

176 that encircles PSI dimers and monomers, confirming the importance of binding with PSI trimers in shaping

177 IsiA assemblies. The distances between the inner and outer rings of IsiA−PSI double-ring and triple-ring

178 complexes as well as between adjacent rings of the IsiA-only assemblies are relatively identical (5.0 ± 0.2

179 nm, $n = 18$) (Fig. 4d), probably essential for efficient energy transfer. Based on the AFM results and cryo-

180 EM of the IsiA−PSI supercomplex, the structural models of the PSI trimer associated with IsiA double rings

181 and triple rings were built (Fig. 4e).

182   Strikingly, IsiA proteins could also self-assemble to form, for example, a helical "stripe" surrounding

183 the central PSI (Supplementary Fig. 7a), the "S-shape" fibres formed by IsiA oligomers to connect two

184 adjacent IsiA−PSI supercomplexes (Supplementary Fig. 7b), the "storm-like" IsiA assemblies around one

185 PSI (Supplementary Fig. 7c), and the insertion of IsiA fibres into the centre of adjacent IsiA−PSI

186 supercomplex through the gap among IsiA assemblies (Supplementary Fig. 7d). The highly variable

187 structures of IsiA assemblies in nature may suggest the plastic IsiA−IsiA and IsiA−PSI interactions *in vivo*

188 and the sequential multistep formation of the IsiA−PSI supercomplex.

189

190 **Structural variability of IsiA−PSI supercomplexes in the iron-starved thylakoid membranes**

191 To investigate whether the organisational heterogeneity of IsiA−PSI supercomplexes in thylakoid

192 membranes is specific to HL adaptation or it also occurs in iron-deficiency conditions, we conducted AFM

193 imaging on the Fe- adapted thylakoid membranes. Consistent with the organisation of the HL-adapted

194 thylakoid membranes, IsiA proteins were densely packed in the Fe- adapted thylakoid membranes and

195 formed various IsiA−PSI supercomplexes that differ in the number of IsiA rings and PSI oligomeric states

196 (Supplementary Fig. 8), indicating that the structural variability is a generic feature of IsiA−PSI assemblies

197 under different stress conditions. The proportion of IsiA−PSI supercomplexes surrounded by a single IsiA

198 ring was declined in the Fe- adapted membranes compare to the HL-adapted membranes, while the

199 proportion of IsiA−PSI supercomplexes with more IsiA rings was increased (Supplementary Table 2), due to

200 the drastic increase of IsiA abundance in the Fe- adapted thylakoid membranes (Supplementary Fig. 2a, 2b).

201 The higher expression of IsiA under iron starvation compared to HL also led to the formation of more IsiA-

202 enriched assemblies in thylakoid membranes (Supplementary Fig. 8).

203

204 **Physiological roles of IsiA**

205 To investigate the function of IsiA, we monitored the P700 oxidation kinetics of Syn7942 cells grown under

206 ML, HL, and Fe- conditions. The k-values of the HL-and Fe- grown cells, which correlate with the PSI

207 absorption cross-section[32,33], were similar and were ~25% higher than the k-value of the ML-grown cells (Fig.

208 5a), indicating that the binding of IsiA to PSI increased the absorption cross-section and antenna size of PSI

209 complexes. The maximum amount of photo-oxidised P700 (P_m) of the HL- and Fe- grown cells were both

210 lower than that of the ML-grown cells (Fig. 5b), and the changes in P_m is roughly consistent with the changes

211 in PSI content under the corresponding conditions (Supplementary Fig. 2a, 2b), implying the main role of the

212 PSI-associated IsiA in photosynthetic light harvesting. Moreover, 77K fluorescence emission spectra

213 (excited at 435 nm) of the HL-grown cells showed a peak at 720 nm corresponding to PSI (Fig. 5c), further

214 confirming the light-harvesting function of IsiA under HL. 77K emission spectra (excited at 435 nm and 600

215 nm) also revealed that the Fe- grown cells exhibit a fluorescence peak at 685 nm (Fig. 5c, 5d), representing

216 IsiA accumulation[34]. As a higher amount of IsiA were expressed under Fe- than ML and HL (Supplementary

217 Fig. 2a, b), we assume that the notable IsiA fluorescence could originate from the excess pool of

218 bioenergetically-decoupled IsiA that are located at the periphery of IsiA−PSI supercomplexes or IsiA-only

219 assemblies (Supplementary Fig. 8, Supplementary Table 2). We also found that cells that lack IsiA grew

220 slower than the Syn7942 WT when transferred from ML to HL (Supplementary Fig. 9). Together, our data

221 indicate that the IsiA proteins that strongly bind with PSI function as an antenna to increase PSI absorption

222 cross-section, consistent with *in vitro* measurements[12], whereas the IsiA proteins that are far from PSI are

223 functionally decoupled with PSI and highly fluorescent, and thus might have the function of Chl storage

224 during the loss of photosystems under stress conditions.

225

226 **Supramolecular organisation of PSI, PSII and Cyt b_6f in thylakoid membranes**

227 Despite that a majority of thylakoid membrane fragments expose their cytoplasmic surface to AFM probes,

228 we also performed high-resolution AFM imaging on the lumen surface of cyanobacterial thylakoids, as

229 indicated by the absence of PSI cytoplasmic protrusions and the presence of PSI lumenal features (Fig. 6).

230 Dimeric protrusions were the predominant features identified in the lumen surface of ML-adapted thylakoid

231 membranes (Fig. 6a, 6b). These dimers could be divided into two groups, one of which has a larger peak-to-

232 peak distance of protrusions (8.9 ± 0.9 nm, $n = 15$) than the other with reduced distance between peaks ($6.2 \pm$

233 0.7 nm, $n = 15$) (Fig. 6c), reminiscent of PSII (PDB: 3WU2) and Cyt b_6f (PDB: 2E74) dimers, respectively

234 (Fig. 6d). Therefore, the dimers with a larger separation of protrusions were assigned to be PSII dimers and

235 the dimers with a smaller separation of protrusions were assigned to be Cyt b_6f dimers. During AFM tip

236 scanning, PSII protrusions above the thylakoid lumen surface were more stable than the PSI protrusions on

237   the cytoplasmic surface (Supplementary Fig. 10), suggesting the relatively strong interactions between the

238   PSII core and extrinsic PsbO, PsbP, PsbQ, PsbU, and PsbV subunits.

239   The lumenal structure of PSI complexes (Fig. 6b, circles) exhibits no significant protrusions in

240   contrast to PSII and Cyt b_6f lumen sides. The PSI trimer has a diameter of 19.0 nm, consistent with the PSI

241   crystal structure (PDB: 1JB0)[30] (Fig. 6d). PSII and Cyt b_6f dimers are interspersed with PSI complexes and

242   the local contacts between individual membrane complexes ensure the formation of PSII−Cyt b_6f−PSI

243   clusters to facilitate photosynthetic linear electron flow (Fig. 6e). There are various binding patterns of PSI

244   and Cyt b_6f complexes (Supplementary Fig. 11), suggesting that the contacting domains of the two

245   membrane complexes are flexible. Variable orientations of PSI and Cyt b_6f have also been reported in the

246   isolated PSI−Cyt b_6f complexes from *Arabidopsis*[35]. By contrast, only one form of PSI−Cyt b_6f association

247   was reported in *Chlamydomonas*[36].

248   In some membrane regions, parallel arrays of PSII dimers were visualised from the cytoplasmic

249   surface (Fig. 6f, 6g, Supplementary Fig. 12), reminiscent of cryo-electron tomography results[37]. The centre-

250   to-centre distance between two coupled dimers within the same row is 11.1 ± 0.7 nm ($n = 5$) (Fig. 6h),

251   consistent with the space between PSII dimers in the crystal lattice (11.6 nm)[38]. The distance between the

252   two protrusions of the dimeric structure is 10.6 nm and the vertical protrusion from the membrane surface is

253   1.3 nm (Fig. 6h), in good agreement with the dimension of PSII dimers at the cytoplasmic side (PDB:

254   3WU2)[39]. It is generally considered that the phycobilisome cores dock predominately on the cytoplasmic

255   surface of PSII[40]. The crystallised arrays of PSII dimers indicate that the phycobilisomes that tightly bind

256   with these PSII dimers form arrays on the thylakoid surface. The angle between the extension of PSII arrays

257   and the direction perpendicular to PSII dimer long axis is 34° (Fig. 6i), important for docking of

258   phycobilisomes to PSII to form phycobilisome arrays[41]. EM images of the isolated phycobilisome-attached

259   thylakoid membranes showed the ordered arrays of phycobilisomes on thylakoid membranes (Supplementary

260   Fig. 12a-12d), similar to the observations of Syn6803 cells[37]. The less-ordered arrangement of

261   phycobilisomes on thylakoid surface was also discerned (Supplementary Fig. 12c, 12d), suggesting the

262   disordered PSII organisation (Fig. 6e).

263   The PSI trimers and dimers around the rows of PSII dimers have close contacts with PSII dimers,

264   implying the possibility of PSII−PSI supercomplex formation in native thylakoid membranes (Fig. 6g, 6i).

265   Based on the AFM topographs, we proposed the structural models of PSI and PSII associations in the local

266   thylakoid membrane environment to elucidate the potential interactions of phycobilisomes with PSI and PSII

267   (Supplementary Fig. 13). One model shows a PSII dimer closely associated with several PSI complexes

268   (Supplementary Fig. 13a, 13b), and the other displays a PSII dimer array surrounded by PSI complexes

269   (Supplementary Fig. 13c, 13d). Docking of phycobilisomes on the photosynthetic complex clusters indicates

270   the possible organisation of phycobilisome-PSII-PSI megacomplexes[22], shedding light on the regulatory

271   mechanism of state transitions. Within the phycobilisome-PSII-PSI megacomplex, for example in Syn6803,

272   excitation energy captured by the phycobilisome is transferred from the allophycocyanin core to PSII

273   through the terminal emitter ApcE, or to PSI through the terminal emitter ApcD[40,42]. Control of energy

274   transfer could be accomplished by the local conformational changes of photosynthetic complexes. The close

275   contacts between PSII and PSI complexes may also provide a means for the "spillover" of excitation energy

276   from PSII to PSI. The dynamic organisations of photosynthetic complexes and the regulatory mechanisms of

277   state transition remain to be further investigated.

278

279   **ATPase-like structures**

280   AFM visualised many ring-like structures in the ML-, HL- and Fe- adapted thylakoid membranes (Fig. 1, 7a,

281   Supplementary Fig. 4, 6, 8). These ring structures had no specific distribution patterns in thylakoid

282   membranes and no defined binding with adjacent IsiA−PSI complexes (Fig. 7b). The outer diameter and the

283   peak-to-peak diameter of the ring-like structure were 7.37 ± 0.24 nm ($n = 31$) and 4.6 ± 0.2 nm ($n = 24$),

284   respectively, and the protrusion of the ring structure from the cytoplasmic thylakoid surface was 1.2 ± 0.2

285   nm ($n = 15$), which was 0.41 ± 0.25 nm ($n = 15$) higher than IsiA (Fig. 7c, 7d). These features are consistent

286   with the dimensions of the C_{14} ring of ATPase[43,44]. Likewise, 14-fold symmetrised correlation average AFM

287   topograph of the ring structure (Fig. 7e) resembles the cryo-EM structure and AFM topographs of isolated

288   ATPase complexes from chloroplasts[43,44] and cyanobacteria[45]. Based on these features, the ring structures

289   were tentatively assigned to be the F_0 domain of ATPase in Syn7942. It is possible that the F_1 heads of

290   ATPases that have a high protrusion from the membrane surface were swept away by AFM probes, as the

291   immunoblot analysis confirmed the presence of the F_1 domain in the isolated thylakoid membranes used for

292   AFM imaging (Supplementary Fig. 2c).

293   In mitochondria, the dimerisation of ATPases was thought to induce the local membrane curvature[46].

294   We found that ATPases in cyanobacterial thylakoid membranes are predominantly monomers

11

295   (Supplementary Fig. 14), consistent with the ATPases in plant thylakoids[47]. Two tightly contacted ATPases

296   were occasionally discerned close to slightly curved membrane regions (Fig. 7b, black arrows). The ATPase

297   complexes could interact tightly with PSI complexes (Fig. 1c, arrows). In the HL-adapted and Fe- adapted

298   thylakoid membranes, ATPases could either associate with PSI complexes directly (Fig. 7b) or bind to IsiA

299   assemblies of the IsiA−PSI supercomplex (Fig. 1g, 7c, Supplementary Fig. 15, 16), indicating the structural

300   and functional links between ATPases and PSI, as well as the flexible binding of ATPases with PSI and IsiA.

301

302   **PSI−NDH-1 supercomplexes**

303   We also observed another type of membrane supercomplexes in proximity to PSI complexes in thylakoid

304   membranes (Fig. 8a, Supplementary Fig. 16). On the cytoplasmic surface, the supercomplex consists of a

305   highly protruding domain in one end and four small protrusions in the other end (Fig. 8b, blue arrows),

306   reminiscent of the structure of cyanobacterial NDH-1 complexes[48,49]. The four membrane domains possess a

307   higher protrusion than IsiA proteins (0.4 nm) and are aligned in a line (Fig. 8c), making these structures

308   distinguishable from IsiA assemblies. The spaces between the four lower-protruding domains are 6.0 nm, 3.7

309   nm, and 3.6 nm, respectively (Fig. 8c), in agreement with the cryo-EM structure of NDH-1 membrane

310   domains (PDB: 6HUM)[48] (Fig. 8d). The overall AFM topograph of the multi-domain complex is highly

311   consistent with the simulated structure based on the cyanobacterial NDH-1 cryo-EM results (Fig. 8e). Thus,

312   these macromolecular structures were assigned as the NDH-1 complexes.

313   The height of the strongly protruded domains varies from 1 nm to 5 nm (Fig. 8c, 8g), consistent with

314   the height of the hydrophilic arm of cyanobacterial NDH-1, which comprises NdhH, I, J, M, N, O, and S

315   subunits[48,49]. Some NDH-1 structures have two protruding domains, a larger one that was assigned to be the

316   hydrophilic arm and a smaller one that appears as the Cup domain including CupA, CupB, and CupS

317   subunits[50-53] (Fig. 8f, 8g), resembling the NDH-1MS structure (PDB: 6TJV)[54]. Time-lapse AFM images

318   showed the independent removal of the two protrusions (Fig. 8f-8h), eventually resulting in the exposure of

319   NDH-1 membrane domains to AFM probes. AFM images allowed us to draw a model of the local

320   organisation of IsiA−PSI, IsiA-only assemblies, NDH-1, and ATPases in cyanobacterial thylakoid

321   membranes (Fig. 8i), which may function as a bioenergetic entity to fulfil and optimise photosynthetic linear

322   and cyclic electron flow for ATP and NADPH production.

323   Based on the AFM image, a structural model of the IsiA−PSI−NDH-1 supercomplex is proposed to

324   illustrate the possible electron flow within the photosynthetic supercomplex (Supplementary Fig. 17).

325   Flavodoxin (Fld) or ferredoxin (Fd) accepts electrons from the PsaC subunit of PSI, and Fd binds to the

326   peripheral domain of the NDH-1 hydrophilic arm transferring electrons to plastoquinone (PQ) to produce

327   PQH_2[85,86]. The cyclic electron flow is completed by the transfer of electrons from PQ back to PSI via Cyt b_6f

328   and plastocyanin. The formation of PSI−NDH-1 supercomplexes facilitates cyclic electron flux and is

329   essential for balancing the ATP/NADPH ratio required for the Calvin–Benson cycle.

330   NDH-1 complexes were observed by AFM in both the HL- and ML-adapted thylakoid membranes

331   (Supplementary Fig. 16, 18). In the HL-adapted thylakoid membranes, more NDH-1 complexes were

332   detected (Supplementary Table 1), as HL could induce expression of NDH-1[27]. In the ML-adapted thylakoid

333   membranes, NDH-1 contacts directly with PSI forming the PSI−NDH-1 supercomplex (Supplementary Fig.

334   18) to maintain efficient cyclic electron transport, as suggested in plants and Syn6803[35,55-57]. NDH-1 could

335   bind with PSI complexes or interact with the peripheral IsiA layers of the IsiA−PSI supercomplexes in

336   diverse manners (Supplementary Fig. 16), indicating the variable, intricate association of NDH-1 with PSI

337   and IsiA complexes.

338

339   **Discussion**

340   The cyanobacterial thylakoid membrane provides the natural platform to functionally position and regulate

341   photosynthetic and respiratory protein complexes for efficient energy transfer and dynamic adaption to cope

342   with environmental changes. *In vivo* expression of IsiA has been reported to be regulated by environmental

343   stress factors and different growth stages[6-10,58]. Previous structural studies have focused on the IsiA−PSI

344   complexes induced by iron-deficient conditions[6,7,11,12,15,31,59-62]. HL-induced expression of IsiA has been

345   reported[9], but prior to this study, there was no structural analysis of the IsiA−PSI complexes generated under

346   HL. Unlike the relatively homogeneous IsiA−PSI structures revealed by single-particle EM[6,7,11,12], AFM

347   images revealed the structural variability of IsiA−PSI supercomplexes in the native cyanobacterial thylakoid

348   membranes. PSI trimers, dimers, or monomers could be associated with a single, double, triple, or multiple

349   IsiA rings, indicative of the flexible interaction between IsiA and PSI (Fig. 3b, Supplementary Table 2). IsiA

350   proteins can also self-aggregate to form IsiA-only assemblies in the PSI-rich regions (Fig. 3e, 4d). These

351   observations suggest that the belt of IsiA proteins is unable to alter the aggregation states of PSI complexes.

352　　It is conceivable that the diverse IsiA−PSI complexes in native membranes represent structural intermediates

353　　generated at different growth conditions during the dynamic biogenesis process of IsiA−PSI supercomplexes

354　　and may have different photosynthetic functions. EM of isolated IsiA−PSI complexes so far has only

355　　reported a single or double IsiA encircling PSI[6,7,11,12,15,31], suggesting that the extra IsiA rings may have

356　　relatively weaker interactions with the central IsiA−PSI complex. The flexible interaction and dynamic

357　　assembly were supported by the previous finding that IsiA proteins are mobile in cyanobacterial thylakoid

358　　membranes[63].

359　　　　The exact function of IsiA in cyanobacteria has remained obscure. There are three prevalent

360　　hypotheses for IsiA functions: (1) store the majority of chlorophylls to compensate for the loss of

361　　photosystems[17,64]; (2) serve as an accessory antenna for PSI to increase the light cross-section of

362　　PSI[6,7,12,14,33,65]; (3) dissipate excess excitation energy for photoprotection[9,16,66]. Our spectroscopic results

363　　indicated that IsiA could function as an alternative light-harvesting antenna funnelling energy to PSI under

364　　stress conditions (Fig. 5), consistent with the *in vitro* results[12], and the tight association of IsiA and PSI

365　　complexes increase the absorption cross-section and antenna size per PSI. The upregulation of IsiA and

366　　formation of IsiA−PSI supercomplexes could thus compensate for the great loss of phycobilisomes and PSI

367　　induced by HL and iron stress (Supplementary Fig. 1, 2). As cells grow faster in HL, they may encounter

368　　iron limitations, such as the rate of Fe uptake for production of PSI reaction centres. Substituting IsiA for PSI

369　　could be a general adaptive mechanism to rapid growth, resulting in the reduced demand for Fe and allowing

370　　cyanobacteria to survive in diverse environmental conditions. Moreover, the highly fluorescent, functionally-

371　　decoupled IsiA, probably the peripheral IsiA rings within the IsiA−PSI supercomplexes and IsiA-only

372　　assemblies as observed in AFM (Fig. 3, Supplementary Figs. 5,7,8), might act as a Chl store when losing

373　　photosystems in physiological regulation, which merits further explorations.

374　　　　The phycobilisomes represent membrane-associated light-harvesting antenna in cyanobacteria and red

375　　algae[67-69]. Apart from the light-harvesting function, phycobilisomes also contribute to nitrogen storage and

376　　photoprotection to cope with environmental stress[70,71]. During the evolution of photosynthetic organisms,

377　　phycobilisomes were gradually replaced by membrane-spanning Chl-containing antenna including IsiA and

378　　homologs, signifying the varying stress-response mechanisms of photosynthetic apparatus to enable their

379　　hosting organisms to adapt to the living niches[72].

380   AFM topographs outline the native organisation of photosynthetic apparatus at the long-range scale

381   and local membrane domains. At the sub-micron scale, photosynthetic membrane complexes have the

382   propensity to segregate and form functional domains throughout the Syn7942 thylakoid membranes, such as

383   PSI-enriched regions (Figs. 1-3) and PSII arrays (Fig. 6f, Supplementary Fig. 12), consistent with

384   fluorescence microscopic observations from Syn7942[19] and Syn6803[73] cells. Given the differences between

385   PSI and PSII in their absorption and turnover rates, the lateral segregation of photosystems in thylakoid

386   membranes may provide favourable micro-environments for photosynthetic linear electron flow[18]. In the

387   PSI-enriched membrane regions of Syn7942, PSI trimers display relatively random orientation, reminiscent

388   of our previous study[19] and the PSI organisation in Syn6803[20]. By contrast, PSI trimers in the thylakoid

389   membranes of *Thermosynechococcus elongatus* and *Synechococcus* sp. PCC 7002 are closely packed to form

390   regular lattices[20]. Moreover, previous EM studies have reported the presence of crystalline PSII arrays in

391   thylakoid membranes from Syn6803 after mild detergent solubilisation[74]. To our knowledge, the present

392   study provides the first view of multiple rows of PSII dimers surrounded by PSI complexes in native

393   cyanobacterial thylakoid membranes, without detergent treatment (Fig. 6, Supplementary Fig. 12). The

394   specific PSII organisation is speculated to facilitate the association of phycobilisomes[69,75]. The respiratory

395   NDH-1 and succinate dehydrogenase complexes have also been reported to be clustered in thylakoid

396   membranes to favour respiratory electron flow towards terminal oxidases[27]. Our finding corroborates that the

397   structural heterogeneity and compartmentalisation of bioenergetic membranes are prevalent in prokaryotes

398   and eukaryotes[76-80], providing the structural basis for high-efficiency metabolism and regulation.

399   There is increasing experimental evidence unveiling the formation of supercomplexes in

400   cyanobacterial [21,22,57,81] and chloroplast thylakoids[55,56,82,83], as well as mitochondria[84]. AFM imaging on native

401   membranes permits the visualisation of membrane supercomplexes formed by weak or flexible interactions.

402   We showed that in the Syn7942 thylakoid membranes, some PSI complexes contact directly with PSII, Cyt

403   b_6f, ATPase, and NDH-1. The association of PSI, Cyt b_6f, and PSII dimer arrays (Fig. 6, Supplementary Fig.

404   13) facilitates photosynthetic linear electron flow and the balance of excitation energy transfer from

405   phycobilisomes to PSII or PSI. Consistently, recent studies have suggested the presence of PSII−PSI

406   supercomplexes[21] and the PSII−PSI−phycobilisome megacomplexes[22] from Syn6803. Intermixing of PSII

407   and Cyt b_6f complexes could facilitate exchange of plastoquinol/plastoquinone molecules, thereby efficient

15

408 electron transport from PSII to Cyt b_6f. ATPases also appear in proximity to PSI, indicative of their structural

409 and functional associations.

410 Our AFM topographs also provide the structural evidence of PSI−NDH-1 supercomplexes in thylakoid

411 membranes (Fig. 8, Supplementary Fig. 16-18) and allow us to propose a structural model of PSI−NDH-1

412 supercomplexes to elucidate cyclic electron flow (Supplementary Fig. 17). The close associations between

413 PSI and NDH-1 could abridge the electron transport pathway and increase the rate of cyclic electron

414 transport to balance the cellular ATP/NADPH ratio in cyanobacteria and plants[5755,56,83]. AFM images also

415 revealed diverse forms of PSI−NDH-1 supercomplexes that vary in the binding sites between PSI, IsiA−PSI,

416 and NDH-1 as well as the oligomeric states of PSI (Fig. 8, Supplementary Fig. 16-18), suggesting that the

417 associations between PSI and NDH-1 are highly flexible and dynamic. This observation is supported by the

418 previous finding that the reorganisation of NDH-1 in cyanobacterial thylakoid membranes, through

419 associating with PSI or forming respiratory clusters under different light regimes, may function as a

420 biological "switch" to regulate the prevalence of linear and cyclic electron flow[27].

421 In summary, by applying high-resolution AFM imaging at the near-physiological conditions and

422 biochemical and spectroscopic analysis, we obtain a molecule-level view of the native architecture of

423 cyanobacterial thylakoid membranes. We find that (1) both HL and Fe- could induce expression of IsiA in

424 Syn7942 and the constructed IsiA−PSI supercomplexes possess diverse configurations in thylakoid

425 membranes; (2) IsiA proteins act as an alternative light-harvesting antenna to increase the effective

426 absorption cross-section of PSI; (3) cyanobacterial thylakoid membranes are laterally heterogeneous and

427 compartmentalise electron transport membrane complexes; (3) direct associations of PSI−PSII, PSI−Cyt b_6f,

428 PSI−ATPase, and PSI−NDH-1 indicate their functional coordination and propensity to form bioenergetic

429 supercomplexes. Viewing the structural landscape of cyanobacterial thylakoid membranes highlights the

430 building and regulatory principles of functional photosynthetic apparatus, and will inform bioengineering to

431 enhance photosynthetic performance and bioenergy production. Knowledge of the photosynthetic membrane

432 organisation could be extended to other bacterial membrane systems, as well as chloroplast thylakoid and

433 mitochondrial membranes.

434

435

436 **Methods**

Strains and growth conditions, generation of mutants

Synechococcus elongatus PCC7942 (Syn7942) was cultivated in Multi-Cultivator MC 1000-OD (Photon Systems Instruments) with BG11 or iron-free BG11 medium at 30°C. The culture was bubbled with air and illuminated with constant cool white LEDs (Moderate light (ML): 40 µmol photons·m^{-2}·s^{-1}; high light (HL): 300 µmol photons·m^{-2}·s^{-1})[27-29]. Iron-free BG11 was prepared as described[87]. Iron-deficiency treatment of cells was performed as reported previously[88] with a slight modification. Cells from the mid-logarithmic growth phase iron-replete cultures were pelleted at room temperature, resuspended, and washed sequentially four times with iron-free BG11. The cultures were then resuspended in iron-free BG-11 to OD$_{750}$ = 0.2 and grown under ML.

The *isiA* gene (Synpcc7942_1542) was deleted by replacing the *isiA* gene with spectinomycin resistance cassette following the Redirect strategy[89] based on homologous recombination[90]. Primers used in this work were listed in Supplementary Table 3. To grow the mutant cells, BG-11 medium was supplemented with spectinomycin at 25 µg·mL^{-1}. Segregation of the mutation was confirmed by PCR (Supplementary Fig. 9).

Absorption spectra

Whole-cell absorption spectra were measured at room temperature using a Cary UV-Vis Spectrophotometer (Agilent Technologies). The OD$_{750}$ of cells was adjusted to 0.5 before measurement. Absorption spectra of isolated thylakoid membranes were normalised by the absorption peak at 682 nm.

Thylakoid membrane isolation

Syn7942 cells were pelleted by centrifugation and washed with buffer A (50 mM MES-NaOH, pH 6.5, 5 mM CaCl$_2$, and 10 mM MgCl$_2$)[91]. Cell pellets were resuspended in buffer A containing 25% glycerol and broken by glass bead (212–300 µm in diameter) at 4°C. Phycobilisomes were decoupled from the thylakoid membranes and disassembled in buffer A (Supplementary Fig. 12a, 12b). Crude thylakoid membrane fractions were isolated as described previously[19,92]. To obtain pure thylakoid membranes for AFM imaging, further separation of the membrane fractions was performed in a step sucrose gradient (2.0 M, 1.3 M, 1.0 M, 0.5 M) and centrifuged at 36,200 rpm in Beckman RPS40 rotor for 1 h at 4°C. The Chl-enriched samples at the 1.0-1.3 M sucrose interface were collected and characterised by high-resolution AFM imaging in buffer.

466 No detergent was added during membrane isolation and AFM imaging to ensure the physiological

467 organisation of isolated thylakoid membranes.

468   Phycobilisome-associated thylakoid membranes were isolated following the previous procedure[69,75]

469 with slight modifications. Syn7942 cells were pelleted by centrifugation, washed with buffer PC (0.5 M

470 potassium phosphate, 0.3 M sodium citrate), and resuspended in buffer SPC (0.5 M sucrose, 0.5 M potassium

471 phosphate, 0.3 M sodium citrate). Phycobilisome-thylakoid membrane fractions were isolated using a step

472 sucrose gradient. The samples at the 1.0-1.3 M sucrose interface were collected for EM imaging.

473

474 **Atomic force microscopy (AFM)**

475 Two microliters of thylakoid membrane samples were adsorbed onto freshly cleaved mica surface with 38

476 µL of adsorption buffer (10 mM Tris–HCl, pH 7.5, 150 mM KCl, 25 mM $MgCl_2$) at room temperature for

477 1.5 h. After adsorption, the sample was carefully rinsed with 800 µL imaging buffer (10 mM Tris–HCl, pH

478 7.5, 150 mM $KCl)^{71}$. High-resolution imaging was performed in AC imaging mode in liquid at room

479 temperature using a NanoWizard 3 AFM (JPK) equipped with an ULTRA S scanner and Ultra-Short

480 Cantilever probe (0.3 N·m^{-1}, Nano World) at scan frequencies of 5 Hz using optimised feedback parameters

481 and a resolution of 512 × 512 pixels. The tip spring constant was routinely calibrated. Images were

482 processed with JPK SPM Data Processing (JPK) and ImageJ.

483

484 **Simulation of AFM images**

485 Chimera, ImageJ, and WSxM were used to simulate AFM images of the PSI, PSII, Cyt b_6f, NDH-1

486 complexes and IsiA−PSI supercomplex. The simulation was carried out with sphere models of atomic

487 structures of each complex generated by using the Chimera package[93]. Tagged image file format (TIFF) file

488 of the sphere model was scaled at X and Y dimension and calibrated at Z dimension according to the size of

489 atomic structure by using ImageJ, and imported as text image file. Text file was processed by using the tip-

490 surface dilation option with the tip radius of 0.5 nm in WSxM. The simulated AFM image was then

491 smoothed by Gaussian smooth with a decay distance 20, and the structure above the thylakoid membrane

492 surface was shown by adjusting the Z scale.

493

494 **SDS-polyacrylamide gel electrophoresis (SDS-PAGE), blue native-PAGE, and immunoblot analysis**

495   For denatured electrophoresis, crude thylakoid membrane proteins were denatured as described[13] and were

496   separated by 15% (w/v) SDS-PAGE. For native gel electrophoresis, thylakoid membrane proteins were

497   studied by blue native-PAGE as previously reported[94] with the exception that 3 % DM was used for

498   solubilisation. Precast gradient polyacrylamide gels from 4 to 16% (NativePAGE™, Thermo Fisher) were

499   used to separate protein complexes in their native forms. After electrophoresis, proteins were transferred to a

500   PVDF membrane (Immobilon-P, Millipore) and analysed with the antibodies specific to IsiA (ImmunoGen

501   Biological Technology Co., Ltd), PsaB, PsbA (D1) and ATPase (Agrisera).

502

503   **P700 oxidation kinetics**

504   P700 oxidation kinetics of intact cells was recorded using a pulse amplitude modulated fluorometer Dual-

505   PAM-100 (Walz, Germany). Before measurements, cell suspensions at the Chl concentration of 20 $\mu g \cdot mL^{-1}$

506   were dark-acclimated. To measure the PSI absorption cross-section, P700 was oxidised by a saturating 3 ms

507   620 nm LED light pulse (20 mmol photons$\cdot m^{-2} \cdot s^{-1}$). The oxidation phase was then fitted with 1st-degree

508   exponential function to obtain k-value. The maximal change in the P700 signal (P_m) upon transformation of

509   P700 from fully reduced to fully oxidised states was achieved by applying a saturation pulse (5000 μm

510   photons$\cdot m^{-2} \cdot s^{-1}$) on the strong far red (720 nm, 75 $W \cdot m^{-2}$) background illumination. Five independent

511   cultures were measured.

512

513   **77K fluorescence spectra**

514   The 77K fluorescence emission spectra of intact cells were measured using a Perkin-Elmer LS50

515   luminescence spectrometer (Foster City, CA) equipped with a liquid-nitrogen sample housing and a red-

516   sensitive photomultiplier. The Chl concentration of the samples was adjusted to 10 $\mu g \cdot mL^{-1}$. Samples frozen

517   in liquid nitrogen were excited with the 435 nm or 600 nm light. Fluorescence emission was recorded in the

518   range of 620-750 nm. The excitation and emission slit widths were 5 nm. Five independent cultures were

519   measured.

520

521   **Mass spectrometry**

522   Isolated thylakoid membranes were washed with PBS buffer and were treated as previously described[95]. 50

523   μg of isolated thylakoid membrane proteins were reconstituted in 25mM ambic and 1% (w/v) Rapigest SF

524 (Waters, UK). Samples were reduced by the addition of 5 mM dithiothreitol (DTT). Protein alkylation was

525 carried out by addition of 10 mM iodoacteamide (IAM) and incubation at RT for 30min in the dark. Excess

526 IAM was quenched by addition of 5 mM DDT. Digestion with trypsin (1:100 trypsin:protein ratio, Promega

527 Gold) was carried overnight at 37°C. Rapigest was then removed by addition of 0.5% (v/v) TFA. Digests

528 were centrifuged at 17,200 g for 30min and the clarified supernatants aspirated. Samples were stage–tipped

529 on C18 filters to remove Chls prior to LC-MSMS analysis. Data-dependent LC-MS/MS analysis was

530 conducted on a QExactive quadrupole-Orbitrap mass spectrometer coupled to a Dionex Ultimate 3000 RSLC

531 nano-liquid chromatograph (Hemel Hempstead, UK). The raw data file was imported into Progenesis QI for

532 Proteomics (Version 3.0 Nonlinear Dynamics, Newcastle upon Tyne, UK, Waters Company). Peak picking

533 parameters were applied with the sensitivity set to maximum and features with charges of 2^+ to 7^+ were

534 retained. A Mascot Generic File, created by Progenesis, was searched against the *Synechococcus elongatus*

535 database from UniProt.

536

537 **Electron microscopy**

538 Isolated phycobilisome-thylakoid membranes were characterised using negative staining transmission

539 electron microscope (TEM). The samples were stained with 3% uranyl acetate. Images were recorded using

540 an FEI Tecnai G2 Spirit BioTWIN transmission electron microscope equipped with a Gatan Rio 16 camera.

541

542

543 **Data availability**

544 The source data underlying Figs. 1c, 2e, 2f, 4a-4d, 5, 6c, 6h, 6d, 7d, 8c, 8g and Supplementary Figs. 1b, 1c,

545 2a-2c, 4b, 4d, 9b, 9d, 12b, 14b and Supplementary Table 1, 2 are provided as a Source Data file. All data are

546 available from the corresponding author upon request.

547

548

549

550 **References**

551 1   Liu, L. N. Distribution and dynamics of electron transport complexes in cyanobacterial thylakoid
552   membranes. *Biochim Biophys Acta* **1857**, 256-265, doi:10.1016/j.bbabio.2015.11.010 (2016).
553 2   Vermaas, W. F. in *Encyclopedia of Life Sciences*   245-251 (Nature Publishing Group, 2001).

554   3   Mullineaux, C. W. Co-existence of photosynthetic and respiratory activities in cyanobacterial thylakoid
555   membranes. *Biochim Biophys Acta* **1837**, 503-511, doi:10.1016/j.bbabio.2013.11.017 (2014).
556   4   Saer, R. G. & Blankenship, R. E. Light harvesting in phototrophic bacteria: structure and function.
557   *Biochem J* **474**, 2107-2131, doi:10.1042/Bcj20160753 (2017).
558   5   Chen, H.-Y. S., Bandyopadhyay, A. & Pakrasi, H. B. Function, regulation and distribution of IsiA, a
559   membrane-bound chlorophyll a-antenna protein in cyanobacteria. *Photosynthetica* **56**, 322-333,
560   doi:10.1007/s11099-018-0787-7 (2018).
561   6   Bibby, T. S., Nield, J. & Barber, J. Iron deficiency induces the formation of an antenna ring around
562   trimeric photosystem I in cyanobacteria. *Nature* **412**, 743-745, doi:Doi 10.1038/35089098 (2001).
563   7   Boekema, E. J. *et al.* A giant chlorophyll-protein complex induced by iron deficiency in cyanobacteria.
564   *Nature* **412**, 745-748, doi:10.1038/35089104 (2001).
565   8   Vinnemeier, J., Kunert, A. & Hagemann, M. Transcriptional analysis of the isiAB operon in salt-
566   stressed cells of the cyanobacterium Synechocystis sp. PCC 6803. *Fems Microbiol Lett* **169**, 323-330,
567   doi:Doi 10.1016/S0378-1097(98)00478-9 (1998).
568   9   Havaux, M. *et al.* The chlorophyll-binding protein IsiA is inducible by high light and protects the
569   cyanobacterium Synechocystis PCC6803 from photooxidative stress. *FEBS Lett* **579**, 2289-2293,
570   doi:10.1016/j.febslet.2005.03.021 (2005).
571   10 Yousef, N., Pistorius, E. K. & Michel, K. P. Comparative analysis of idiA and isiA transcription under
572   iron starvation and oxidative stress in Synechococcus elongatus PCC 7942 wild-type and selected
573   mutants. *Arch Microbiol* **180**, 471-483, doi:10.1007/s00203-003-0618-4 (2003).
574   11 Toporik, H., Li, J., Williams, D., Chiu, P. L. & Mazor, Y. The structure of the stress-induced
575   photosystem I-IsiA antenna supercomplex. *Nat Struct Mol Biol* **26**, 443-449, doi:10.1038/s41594-019-
576   0228-8 (2019).
577   12 Cao, P. *et al.* Structural basis for energy and electron transfer of the photosystem I-IsiA-flavodoxin
578   supercomplex. *Nat Plants* **6**, 167-176, doi:10.1038/s41477-020-0593-7 (2020).
579   13 Ma, F. *et al.* Dynamic Changes of IsiA-Containing Complexes during Long-Term Iron Deficiency in
580   Synechocystis sp PCC 6803. *Molecular Plant* **10**, 143-154, doi:10.1016/j.molp.2016.10.009 (2017).
581   14 Sun, J. L. & Golbeck, J. H. The Presence of the IsiA-PSI Supercomplex Leads to Enhanced
582   Photosystem I Electron Throughput in Iron-Starved Cells of Synechococcus sp PCC 7002. *J Phys Chem
583   B* **119**, 13549-13559, doi:10.1021/acs.jpcb.5b02176 (2015).
584   15 Chauhan, D. *et al.* A novel photosynthetic strategy for adaptation to low-iron aquatic environments.
585   *Biochemistry* **50**, 686-692, doi:10.1021/bi009425 (2011).
586   16 Park, Y. I., Sandstrom, S., Gustafsson, P. & Oquist, G. Expression of the isiA gene is essential for the
587   survival of the cyanobacterium Synechococcus sp. PCC 7942 by protecting photosystem II from excess
588   light under iron limitation. *Mol Microbiol* **32**, 123-129, doi:10.1046/j.1365-2958.1999.01332.x (1999).
589   17 Schoffman, H. & Keren, N. Function of the IsiA pigment-protein complex in vivo. *Photosynth Res*,
590   doi:10.1007/s11120-019-00638-5 (2019).
591   18 Busch, K. B., Deckers-Hebestreit, G., Hanke, G. T. & Mulkidjanian, A. Y. Dynamics of bioenergetic
592   microcompartments. *Biol Chem* **394**, 163-188, doi:10.1515/hsz-2012-0254 (2013).
593   19 Casella, S. *et al.* Dissecting the Native Architecture and Dynamics of Cyanobacterial Photosynthetic
594   Machinery. *Mol Plant* **10**, 1434-1448, doi:10.1016/j.molp.2017.09.019 (2017).
595   20 MacGregor-Chatwin, C. *et al.* Lateral Segregation of Photosystem I in Cyanobacterial Thylakoids.
596   *Plant Cell* **29**, 1119-1136, doi:10.1105/tpc.17.00071 (2017).
597   21 Bečková, M. *et al.* Association of Psb28 and Psb27 proteins with PSII-PSI supercomplexes upon
598   exposure of *Synechocystis* sp. PCC 6803 to high light. *Mol Plant* **10**, 62-72,
599   doi:10.1016/j.molp.2016.08.001 (2017).
600   22 Liu, H. *et al.* Phycobilisomes supply excitations to both photosystems in a megacomplex in
601   cyanobacteria. *Science* **342**, 1104-1107, doi:10.1126/science.1242321 (2013).
602   23 Liu, L. N. & Scheuring, S. Investigation of photosynthetic membrane structure using atomic force
603   microscopy. *Trends Plant Sci* **18**, 277-286, doi:10.1016/j.tplants.2013.03.001 (2013).
604   24 MacGregor-Chatwin, C. *et al.* Membrane organization of photosystem I complexes in the most
605   abundant phototroph on Earth. *Nat Plants* **5**, 879-889, doi:10.1038/s41477-019-0475-z (2019).
606   25 Riediger, M. *et al.* Biocomputational Analyses and Experimental Validation Identify the Regulon
607   Controlled by the Redox-Responsive Transcription Factor RpaB. *iScience* **15**, 316-331,
608   doi:10.1016/j.isci.2019.04.033 (2019).

609 26   Kappell, A. D., Bhaya, D. & van Waasbergen, L. G. Negative control of the high light-inducible hliA
610   gene and implications for the activities of the NblS sensor kinase in the cyanobacterium Synechococcus
611   elongatus strain PCC 7942. *Arch Microbiol* **186**, 403-413, doi:10.1007/s00203-006-0154-0 (2006).
612 27   Liu, L. N. *et al.* Control of electron transport routes through redox-regulated redistribution of respiratory
613   complexes. *Proc Natl Acad Sci U S A* **109**, 11431-11436, doi:10.1073/pnas.1120960109 (2012).
614 28   Sun, Y. *et al.* Light modulates the biosynthesis and organization of cyanobacterial carbon fixation
615   machinery through photosynthetic electron flow. *Plant Physiol* **171**, 530-541, doi:10.1104/pp.16.00107
616   (2016).
617 29   Sun, Y., Wollman, A. J. M., Huang, F., Leake, M. C. & Liu, L. N. Single-organelle quantification
618   reveals the stoichiometric and structural variability of carboxysomes dependent on the environment.
619   *Plant Cell* **31**, 1648-1664 (2019).
620 30   Jordan, P. *et al.* Three-dimensional structure of cyanobacterial photosystem I at 2.5 A resolution. *Nature*
621   **411**, 909-917, doi:10.1038/35082000 (2001).
622 31   Yeremenko, N. *et al.* Supramolecular organization and dual function of the IsiA chlorophyll-binding
623   protein in cyanobacteria. *Biochemistry* **43**, 10308-10313, doi:10.1021/bi0487721 (2004).
624 32   Zipfel, W. & Owens, T. G. Calculation of absolute photosystem I absorption cross-sections from P700
625   photo-oxidation kinetics. *Photosynth Res* **29**, 23-35, doi:10.1007/BF00035203 (1991).
626 33   Ryan-Keogh, T. J., Macey, A. I., Cockshutt, A. M., Moore, C. M. & Bibby, T. S. The cyanobacterial
627   chlorophyll-binding-protein Isia acts to increase the *in vivo* effective absorption cross-section of PSI
628   under iron limitation(1). *J Phycol* **48**, 145-154, doi:10.1111/j.1529-8817.2011.01092.x (2012).
629 34   Odom, W. R., Hodges, R., Chitnis, P. R. & Guikema, J. A. Characterization of Synechocystis sp. PCC
630   6803 in iron-supplied and iron-deficient media. *Plant Mol Biol* **23**, 1255-1264, doi:10.1007/bf00042358
631   (1993).
632 35   Yadav, K. N. *et al.* Supercomplexes of plant photosystem I with cytochrome b6f, light-harvesting
633   complex II and NDH. *Biochim Biophys Acta Bioenerg* **1858**, 12-20, doi:10.1016/j.bbabio.2016.10.006
634   (2017).
635 36   Steinbeck, J. *et al.* Structure of a PSI-LHCI-cyt b6f supercomplex in Chlamydomonas reinhardtii
636   promoting cyclic electron flow under anaerobic conditions. *Proc Natl Acad Sci U S A* **115**, 10517-10522,
637   doi:10.1073/pnas.1809973115 (2018).
638 37   Rast, A. *et al.* Biogenic regions of cyanobacterial thylakoids form contact sites with the plasma
639   membrane. *Nat Plants* **5**, 436-446, doi:10.1038/s41477-019-0399-7 (2019).
640 38   Hellmich, J. *et al.* Native-like photosystem II superstructure at 2.44 A resolution through detergent
641   extraction from the protein crystal. *Structure* **22**, 1607-1615, doi:10.1016/j.str.2014.09.007 (2014).
642 39   Umena, Y., Kawakami, K., Shen, J. R. & Kamiya, N. Crystal structure of oxygen-evolving photosystem
643   II at a resolution of 1.9 A. *Nature* **473**, 55-60, doi:10.1038/nature09913 (2011).
644 40   Chang, L. *et al.* Structural organization of an intact phycobilisome and its association with photosystem
645   II. *Cell Res* **25**, 726-737, doi:10.1038/cr.2015.59 (2015).
646 41   Zlenko, D. V., Galochkina, T. V., Krasilnikov, P. M. & Stadnichuk, I. N. Coupled rows of PBS cores
647   and PSII dimers in cyanobacteria: symmetry and structure. *Photosynth Res* **133**, 245-260,
648   doi:10.1007/s11120-017-0362-2 (2017).
649 42   McConnell, M. D., Koop, R., Vasil'ev, S. & Bruce, D. Regulation of the distribution of chlorophyll and
650   phycobilin-absorbed excitation energy in cyanobacteria. A structure-based model for the light state
651   transition. *Plant Physiol* **130**, 1201-1212, doi:10.1104/pp.009845 (2002).
652 43   Seelert, H., Dencher, N. A. & Müller, D. J. Fourteen Protomers Compose the Oligomer III of the
653   Proton-rotor in Spinach Chloroplast ATP Synthase. *Journal of Molecular Biology* **333**, 337-344,
654   doi:10.1016/j.jmb.2003.08.046 (2003).
655 44   Hahn, A., Vonck, J., Mills, D. J., Meier, T. & Kuhlbrandt, W. Structure, mechanism, and regulation of
656   the chloroplast ATP synthase. *Science* **360**, doi:10.1126/science.aat4318 (2018).
657 45   Pogoryelov, D. *et al.* The oligomeric state of c rings from cyanobacterial F-ATP synthases varies from
658   13 to 15. *J Bacteriol* **189**, 5895-5902, doi:10.1128/JB.00581-07 (2007).
659 46   Strauss, M., Hofhaus, G., Schroder, R. R. & Kuhlbrandt, W. Dimer ribbons of ATP synthase shape the
660   inner mitochondrial membrane. *EMBO J* **27**, 1154-1160, doi:10.1038/emboj.2008.35 (2008).
661 47   Daum, B., Nicastro, D., Il, J. A., McIntosh, J. R. & Kuhlbrandt, W. Arrangement of Photosystem II and
662   ATP Synthase in Chloroplast Membranes of Spinach and Pea. *Plant Cell* **22**, 1299-1312,
663   doi:10.1105/tpc.109.071431 (2010).
664 48   Schuller, J. M. *et al.* Structural adaptations of photosynthetic complex I enable ferredoxin-dependent
665   electron transfer. *Science* **363**, 257-+, doi:10.1126/science.aau3613 (2019).

666 49 Laughlin, T. G., Bayne, A. N., Trempe, J. F., Savage, D. F. & Davies, K. M. Structure of the complex I-
667   like molecule NDH of oxygenic photosynthesis. *Nature* **566**, 411-414, doi:10.1038/s41586-019-0921-0
668   (2019).
669 50 Arteni, A. A. *et al.* Structural characterization of NDH-1 complexes of Thermosynechococcus elongatus
670   by single particle electron microscopy. *Biochim Biophys Acta* **1757**, 1469-1475,
671   doi:10.1016/j.bbabio.2006.05.042 (2006).
672 51 Folea, I. M. *et al.* Single particle analysis of thylakoid proteins from Thermosynechococcus elongatus
673   and Synechocystis 6803: localization of the CupA subunit of NDH-1. *FEBS Lett* **582**, 249-254,
674   doi:10.1016/j.febslet.2007.12.012 (2008).
675 52 Birungi, M. *et al.* Possibilities of subunit localization with fluorescent protein tags and electron
676   microscopy examplified by a cyanobacterial NDH-1 study. *Biochim Biophys Acta* **1797**, 1681-1686,
677   doi:10.1016/j.bbabio.2010.06.004 (2010).
678 53 Peltier, G., Aro, E. M. & Shikanai, T. NDH-1 and NDH-2 Plastoquinone Reductases in Oxygenic
679   Photosynthesis. *Annu Rev Plant Biol* **67**, 55-80, doi:10.1146/annurev-arplant-043014-114752 (2016).
680 54 Schuller, J. M. *et al.* Redox-coupled proton pumping drives carbon concentration in the photosynthetic
681   complex I. *Nature Communications* **11**, 494, doi:10.1038/s41467-020-14347-4 (2020).
682 55 Kouril, R. *et al.* Structural characterization of a plant photosystem I and NAD(P)H dehydrogenase
683   supercomplex. *Plant J* **77**, 568-576, doi:10.1111/tpj.12402 (2014).
684 56 Peng, L., Fukao, Y., Fujiwara, M., Takami, T. & Shikanai, T. Efficient operation of NAD(P)H
685   dehydrogenase requires supercomplex formation with photosystem I via minor LHCI in Arabidopsis.
686   *Plant Cell* **21**, 3623-3640, doi:10.1105/tpc.109.068791 (2009).
687 57 Gao, F. *et al.* The NDH-1L-PSI Supercomplex Is Important for Efficient Cyclic Electron Transport in
688   Cyanobacteria. *Plant Physiol* **172**, 1451-1464, doi:10.1104/pp.16.00585 (2016).
689 58 Singh, A. K. & Sherman, L. A. Iron-independent dynamics of IsiA production during the transition to
690   stationary phase in the cyanobacterium Synechocystis sp. PCC 6803. *FEMS Microbiol Lett* **256**, 159-
691   164, doi:10.1111/j.1574-6968.2006.00114.x (2006).
692 59 Bibby, T. S., Nield, J. & Barber, J. Three-dimensional model and characterization of the iron stress-
693   induced CP43'-photosystem I supercomplex isolated from the cyanobacterium Synechocystis PCC 6803.
694   *J Biol Chem* **276**, 43246-43252, doi:10.1074/jbc.M106541200 (2001).
695 60 Kouril, R. *et al.* Photosystem I trimers from Synechocystis PCC 6803 lacking the PsaF and PsaJ
696   subunits bind an IsiA ring of 17 units. *Biochim Biophys Acta* **1607**, 1-4,
697   doi:10.1016/j.bbabio.2003.08.002 (2003).
698 61 Aspinwall, C. L., Duncan, J., Bibby, T., Mullineaux, C. W. & Barber, J. The trimeric organisation of
699   photosystem I is not necessary for the iron-stress induced CP43' protein to functionally associate with
700   this reaction centre. *FEBS Lett* **574**, 126-130, doi:10.1016/j.febslet.2004.08.016 (2004).
701 62 Kouril, R. *et al.* Supercomplexes of IsiA and photosystem I in a mutant lacking subunit PsaL. *Biochim
702   Biophys Acta* **1706**, 262-266, doi:10.1016/j.bbabio.2004.11.008 (2005).
703 63 Sarcina, M. & Mullineaux, C. W. Mobility of the IsiA chlorophyll-binding protein in cyanobacterial
704   thylakoid membranes. *J Biol Chem* **279**, 36514-36518, doi:10.1074/jbc.M405881200 (2004).
705 64 Riethman, H. C. & Sherman, L. A. Purification and characterization of an iron stress-induced
706   chlorophyll-protein from the cyanobacterium Anacystis nidulans R2. *Biochim Biophys Acta* **935**, 141-
707   151, doi:10.1016/0005-2728(88)90211-3 (1988).
708 65 Burnap, R. L., Troyan, T. & Sherman, L. A. The highly abundant chlorophyll-protein complex of iron-
709   deficient Synechococcus sp. PCC7942 (CP43') is encoded by the isiA gene. *Plant Physiol* **103**, 893-902,
710   doi:10.1104/pp.103.3.893 (1993).
711 66 Sandstrom, S., Park, Y. I., Oquist, G. & Gustafsson, P. CP43', the isiA gene product, functions as an
712   excitation energy dissipator in the cyanobacterium Synechococcus sp. PCC 7942. *Photochem Photobiol*
713   **74**, 431-437 (2001).
714 67 Zhang, J. *et al.* Structure of phycobilisome from the red alga Griffithsia pacifica. *Nature* **551**, 57-63,
715   doi:10.1038/nature24278 (2017).
716 68 Liu, L. N., Chen, X. L., Zhang, Y. Z. & Zhou, B. C. Characterization, structure and function of linker
717   polypeptides in phycobilisomes of cyanobacteria and red algae: An overview. *Biochimica et Biophysica
718   Acta-Bioenergetics* **1708**, 133-142, doi:10.1016/j.bbabio.2005.04.001 (2005).
719 69 Arteni, A. A. *et al.* Structure and organization of phycobilisomes on membranes of the red alga
720   *Porphyridium cruentum*. *Photosynth Res* **95**, 169-174, doi:10.1007/s11120-007-9264-z (2008).
721 70 Liu, L. N. *et al.* Light-induced energetic decoupling as a mechanism for phycobilisome-related energy
722   dissipation in red algae: a single molecule study. *PLoS ONE* **3**, e3134 (2008).

723   71   Zhao, L. S. *et al.* Supramolecular architecture of photosynthetic membrane in red algae in response to
724   nitrogen starvation. *Biochim Biophys Acta* **1857**, 1751-1758, doi:10.1016/j.bbabio.2016.08.005 (2016).
725   72   Green, B. R. What Happened to the Phycobilisome? *Biomolecules* **9**, doi:10.3390/biom9110748 (2019).
726   73   Straskova, A. *et al.* Pigment-protein complexes are organized into stable microdomains in
727   cyanobacterial thylakoids. *Biochim Biophys Acta Bioenerg*, doi:10.1016/j.bbabio.2019.07.008 (2019).
728   74   Folea, I. M., Zhang, P., Aro, E. M. & Boekema, E. J. Domain organization of photosystem II in
729   membranes of the cyanobacterium *Synechocystis* PCC6803 investigated by electron microscopy. *FEBS*
730   *Lett* **582**, 1749-1754, doi:10.1016/j.febslet.2008.04.044 (2008).
731   75   Liu, L. N. *et al.* Watching the native supramolecular architecture of photosynthetic membrane in red
732   algae: topography of phycobilisomes and their crowding, diverse distribution patterns. *J Biol Chem* **283**,
733   34946-34953, doi:10.1074/jbc.M805114200 (2008).
734   76   Lenn, T., Leake, M. C. & Mullineaux, C. W. Clustering and dynamics of cytochrome *bd*-I complexes in
735   the *Escherichia coli* plasma membrane *in vivo*. *Mol Microbiol* **70**, 1397-1407, doi:10.1111/j.1365-
736   2958.2008.06486.x (2008).
737   77   Llorente-Garcia, I. *et al.* Single-molecule *in vivo* imaging of bacterial respiratory complexes indicates
738   delocalized   oxidative   phosphorylation.   *Biochim   Biophys   Acta*   **1837**,   811-824,
739   doi:10.1016/j.bbabio.2014.01.020 (2014).
740   78   Johnson, A. S., van Horck, S. & Lewis, P. J. Dynamic localization of membrane proteins in *Bacillus*
741   *subtilis*. *Microbiology* **150**, 2815-2824, doi:10.1099/mic.0.27223-0 (2004).
742   79   Cornejo, E., Abreu, N. & Komeili, A. Compartmentalization and organelle formation in bacteria. *Curr*
743   *Opin Cell Biol* **26**, 132-138, doi:10.1016/j.ceb.2013.12.007 (2014).
744   80   Vogel, F., Bornhovd, C., Neupert, W. & Reichert, A. S. Dynamic subcompartmentalization of the
745   mitochondrial inner membrane. *J Cell Biol* **175**, 237-247, doi:10.1083/jcb.200605138 (2006).
746   81   Watanabe, M. *et al.* Attachment of phycobilisomes in an antenna-photosystem I supercomplex of
747   cyanobacteria. *Proc Natl Acad Sci U S A* **111**, 2512-2517, doi:10.1073/pnas.1320599111 (2014).
748   82   Iwai, M. *et al.* Isolation of the elusive supercomplex that drives cyclic electron flow in photosynthesis.
749   *Nature* **464**, 1210-1213, doi:10.1038/nature08885 (2010).
750   83   Peng, L., Shimizu, H. & Shikanai, T. The chloroplast NAD(P)H dehydrogenase complex interacts with
751   photosystem I in Arabidopsis. *J Biol Chem* **283**, 34873-34879, doi:10.1074/jbc.M803207200 (2008).
752   84   Lapuente-Brun, E. *et al.* Supercomplex assembly determines electron flux in the mitochondrial electron
753   transport chain. *Science* **340**, 1567-1570, doi:10.1126/science.1230381 (2013).
754   85   Pan, X. *et al.* Structural basis for electron transport mechanism of complex I-like photosynthetic
755   NAD(P)H dehydrogenase. *Nat Commun* **11**, 610, doi:10.1038/s41467-020-14456-0 (2020).
756   86   Zhang, C. *et al.* Structural insights into NDH-1 mediated cyclic electron transfer. *Nature*
757   *communications* **11**, 888-888, doi:10.1038/s41467-020-14732-z (2020).
758   87   Katoh, H., Grossman, A. R., Hagino, N. & Ogawa, T. A gene of Synechocystis sp strain PCC 6803
759   encoding   a   novel   iron   transporter.   *Journal   of   Bacteriology*   **182**,   6523-6524,   doi:Doi
760   10.1128/Jb.182.22.6523-6524.2000 (2000).
761   88   Wang, Q., Hall, C. L., Al-Adami, M. Z. & He, Q. IsiA is required for the formation of photosystem I
762   supercomplexes and for efficient state transition in synechocystis PCC 6803. *PLoS One* **5**, e10432,
763   doi:10.1371/journal.pone.0010432 (2010).
764   89   Gust, B., Kieser, T. & Chater, K. F. *REDIRECT Technology: PCR-targeting System in Streptomyces*
765   *coelicolor*. (John Innes Centre, 2002).
766   90   Huang, F. *et al.* Roles of RbcX in carboxysome biosynthesis in the cyanobacterium *Synechococcus*
767   *elongatus* PCC7942. *Plant Physiol* **179**, 184-194, doi:10.1104/pp.18.01217 (2019).
768   91   Li, M., Semchonok, D. A., Boekema, E. J. & Bruce, B. D. Characterization and Evolution of Tetrameric
769   Photosystem I from the Thermophilic Cyanobacterium Chroococcidiopsis sp TS-821. *Plant Cell* **26**,
770   1230-1245, doi:10.1105/tpc.113.120782 (2014).
771   92   Zhang, P. P. *et al.* Expression and functional roles of the two distinct NDH-1 complexes and the carbon
772   acquisition complex NdhD3/NdhF3/CupA/Sll1735 in Synechocystis sp PCC 6803. *Plant Cell* **16**, 3326-
773   3340, doi:DOI 10.1105/tpc.104.026526 (2004).
774   93   Pettersen, E. F. *et al.* UCSF Chimera--a visualization system for exploratory research and analysis. *J*
775   *Comput Chem* **25**, 1605-1612, doi:10.1002/jcc.20084 (2004).
776   94   Zhang, P. P. *et al.* Operon flv4-flv2 Provides Cyanobacterial Photosystem II with Flexibility of Electron
777   Transfer. *Plant Cell* **24**, 1952-1971, doi:10.1105/tpc.111.094417 (2012).
778   95   Faulkner, M. *et al.* Direct characterization of the native structure and mechanics of cyanobacterial
779   carboxysomes. *Nanoscale* **9**, 10662–10673, doi:10.1039/C7NR02524F (2017).

24

781 **Correspondence and requests for materials** should be addressed to L.-N.L. or Y.-Z.Z.

782

798

799

800 **Author contributions**

801 L.-S.Z., Y.-Z.Z. and L.-N.L. conceived the project; L.-S.Z., T.H., S.W., D.M.S., C.W.M., and L.-N.L.

802 performed the research; L.-S.Z., T.H. S.W., D.M.S., Q.W., A.V.R., C.W.M., Y.-Z.Z. and L.-N.L. analysed

803 the data; L.-S.Z., T.H., C.W.M., Y.-Z.Z. and L.-N.L. wrote the manuscript. All of the authors discussed and

804 commented on the results and the manuscript.

805

806

807 **Competing interests**

808 The authors declare no conflict of interest.

809
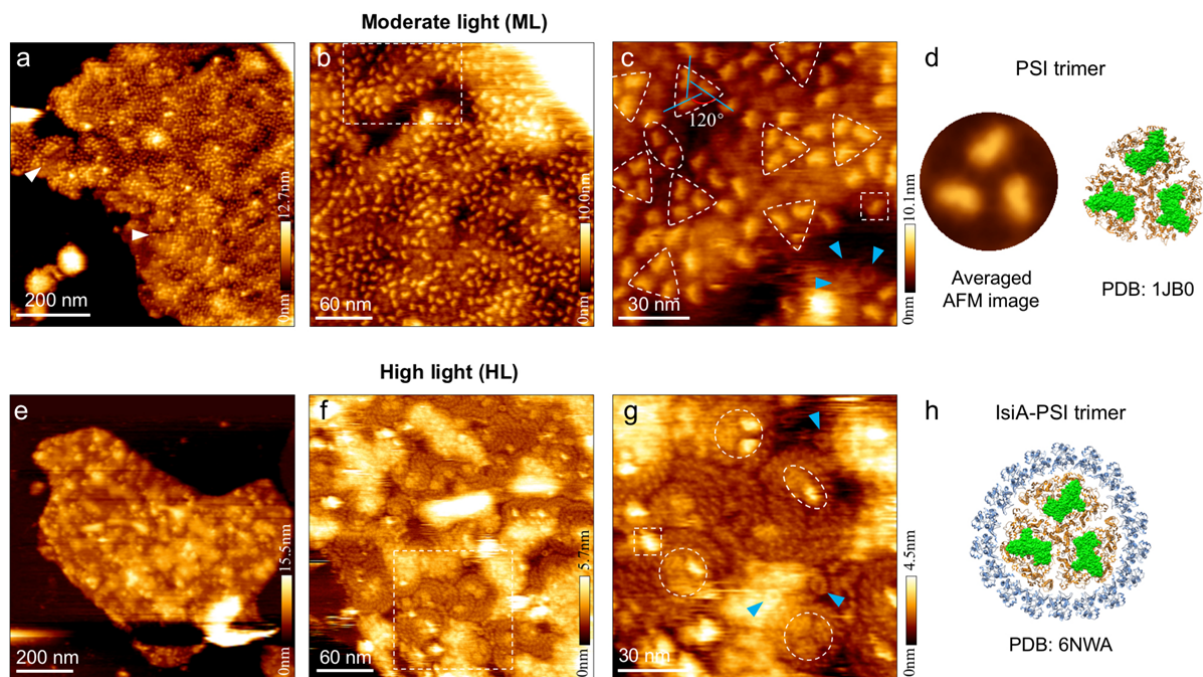
Fig. 1. AFM images of native thylakoid membranes from the ML- and HL- adapted Syn7942 cells. a, AFM topograph of the ML-adapted thylakoid membrane fragment in liquid showing the densely packed photosynthetic membrane proteins. Structures with the ordered organisation are indicated by arrows. **b**, High-resolution AFM image of the cytoplasmic surface of ML thylakoid membrane showing the crowded arrangement of photosynthetic membrane proteins more clearly. The area represented by the white box is shown in **c**. **c**, Zoon-in view of the area highlighted in **b** showing the trimeric (triangle), dimeric (oval) and monomeric (square) PSI complexes in detail. The angle between the long axes of the three protrusions is shown by blue solid line. Small ring structures speculated to be ATPase membrane domains are highlighted with blue arrows. **d**, The three-fold symmetrised correlation averaged AFM topograph of PSI from the cytoplasmic surface of thylakoid membranes (left). Atomic structure of the trimeric PSI complex from the cytoplasmic surface (right, PDB: 1JB0). The subunits (PsaC, PsaD, PsaE) in green are the domains protruding above the membrane surface. **e**, AFM topograph of the HL-adapted thylakoid membrane fragment in liquid. **f**, High-resolution AFM image of the cytoplasmic surface of HL thylakoid membrane showing the densely packed photosynthetic membrane proteins more clearly. The area delineated by the white box is shown in **g**. **g**, Zoon-in view of the area highlighted in **f** showing the trimeric (circle), dimeric (oval) and monomeric (square) PSI complexes in more detail. Small ring structures speculated to be ATPase membrane domains are highlighted with blue arrows. **h**, Atomic structure of the IsiA−PSI supercomplex from the cytoplasmic surface (PDB: 6NWA). The subunits (PsaC, PsaD, PsaE) in green are the domains protruding above the membrane surface. The representative AFM imaging was shown from at least five biologically independent membrane preparations.
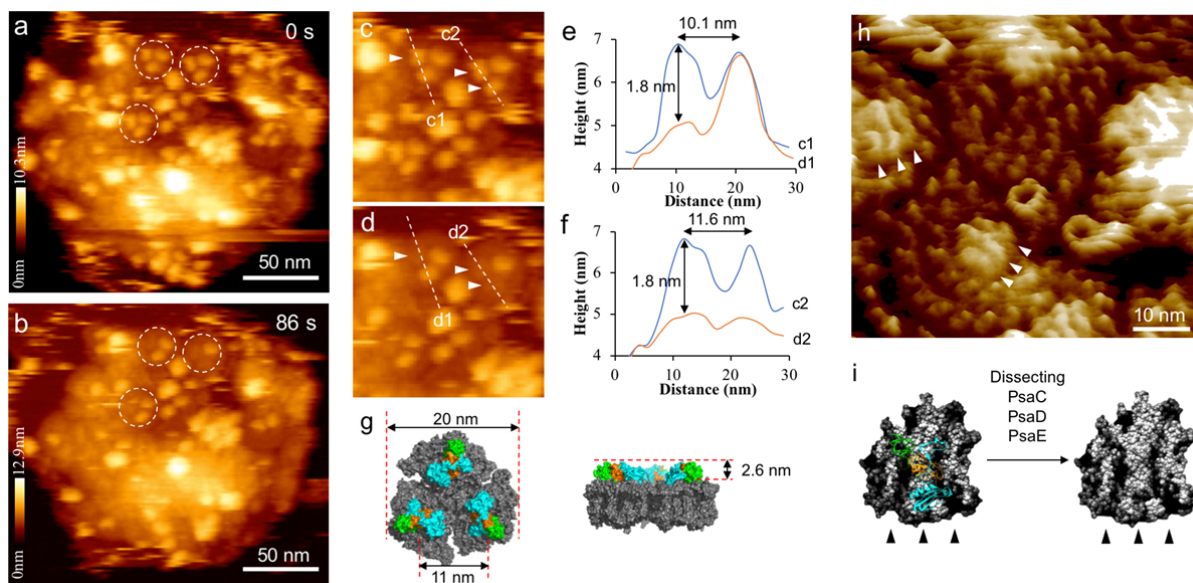
**Fig. 2. Removal of the cytoplasmic subunits of PSI by AFM nanodissection. a**, The first scan of a HL-adapted thylakoid membrane fragment by AFM. Trimeric PSI complexes are highlighted with circles. **b**, The second scan of the same fragment as shown in **a**. Same trimeric PSI complexes are also highlighted with circles. **c**, Zoom-in view of the three trimeric PSI complexes circled in **a**. Dashed lines show the positions of height profiles, and the arrows represent three protrusions of PSI complexes. **d**, Zoom-in view of the three trimeric PSI complexes circled in **b**. Dashed lines show the positions of height profiles same as in **c**. Protrusions of PSI complexes shown by arrows in **c** were removed. **e**, Height profiles corresponding to the c1 line in **c** and d1 line in **d**. The lateral distance between peaks is 10.1 nm, and the height difference of PSI complex before and after losing subunits is 1.8 nm. **f**, Height profiles corresponding to the c2 line in **c** and d2 line in **d**. The lateral distance between peaks is 11.6 nm, and the height difference of PSI complex before and after losing subunits is 1.8 nm. **g**, Atomic structure of the trimeric PSI complex from the cytoplasmic surface (PDB: 1JB0). The diameter of the trimeric PSI complex is 21 nm. The distance between the highest positions of PSI monomers is 11 nm, and the height of the subunits [PsaC (orange), PsaD (blue) and PsaE (green)] above membrane surface is 2.6 nm. **h**, High-resolution AFM image of the cytoplasmic surface of HL-adapted thylakoid membrane showing the PSI surface structure after losing subunits in more detail (arrows). **i**, Atomic structure of the monomeric PSI complex from the cytoplasmic surface (PDB: 1JB0). PsaC (orange), PsaD (blue) and PsaE (green) subunits are removed, and three ridges appear indicated by black arrows. The representative AFM imaging was shown from at least five biologically independent membrane preparations.
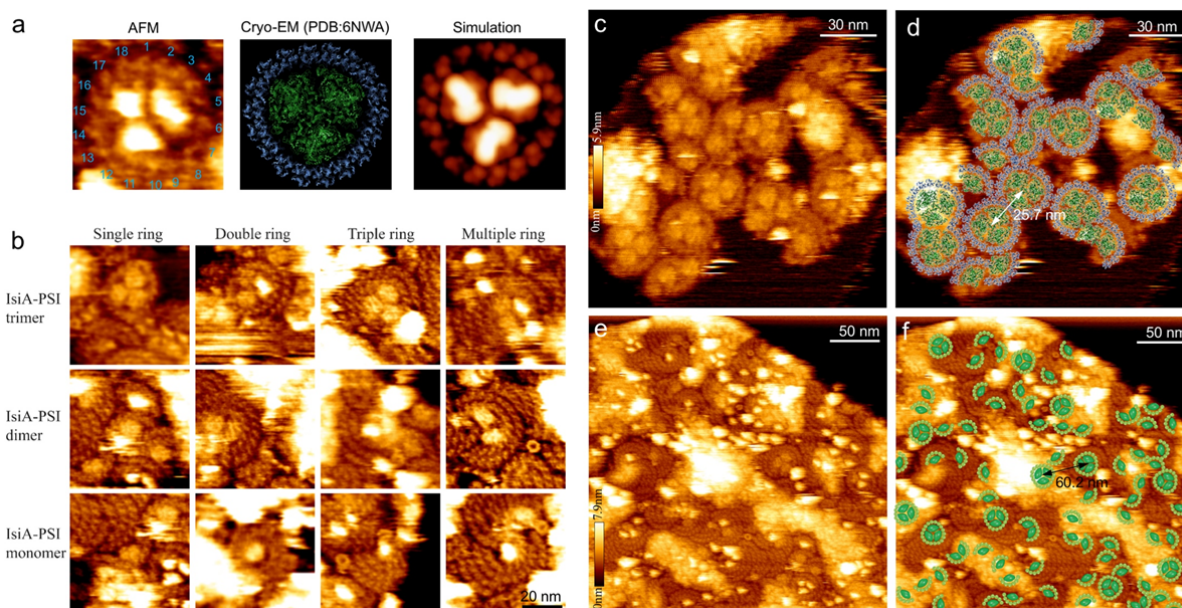
Fig. 3. AFM topographs of thylakoid membranes from HL-adapted Syn7942 cells. a, Zoom-in view of AFM topograph of IsiA−PSI trimer supercomplex showing eighteen IsiA subunits around the PSI trimer (left). Atomic structure of the IsiA−PSI supercomplex from the cytoplasmic surface (middle, PDB: 6NWA). Simulated AFM image of IsiA−PSI supercomplex based on PDB: 6NWA (right). **b**, IsiA−PSI supercomplexes with various numbers of IsiA rings and different PSI oligomerisation states. **c**, AFM topograph of the HL-adapted thylakoid membrane fragment with densely packed IsiA−PSI supercomplexes. **d**, Structural model of the arrangement of IsiA−PSI supercomplexes within the thylakoid membrane in **a** (PDB: 6NWA). The space between two adjacent IsiA−PSI trimer supercomplexes is 25.7 nm. **e**, AFM topograph of the HL-adapted thylakoid membrane fragment with densely packed IsiA proteins. PSI complexes intersperse throughout the membrane. **f**, Model of the arrangement IsiA−PSI supercomplexes within the thylakoid membrane in **c**. The distance between two close IsiA−PSI trimer supercomplexes is 60.2 nm. The representative AFM imaging was shown from at least five biologically independent membrane preparations.
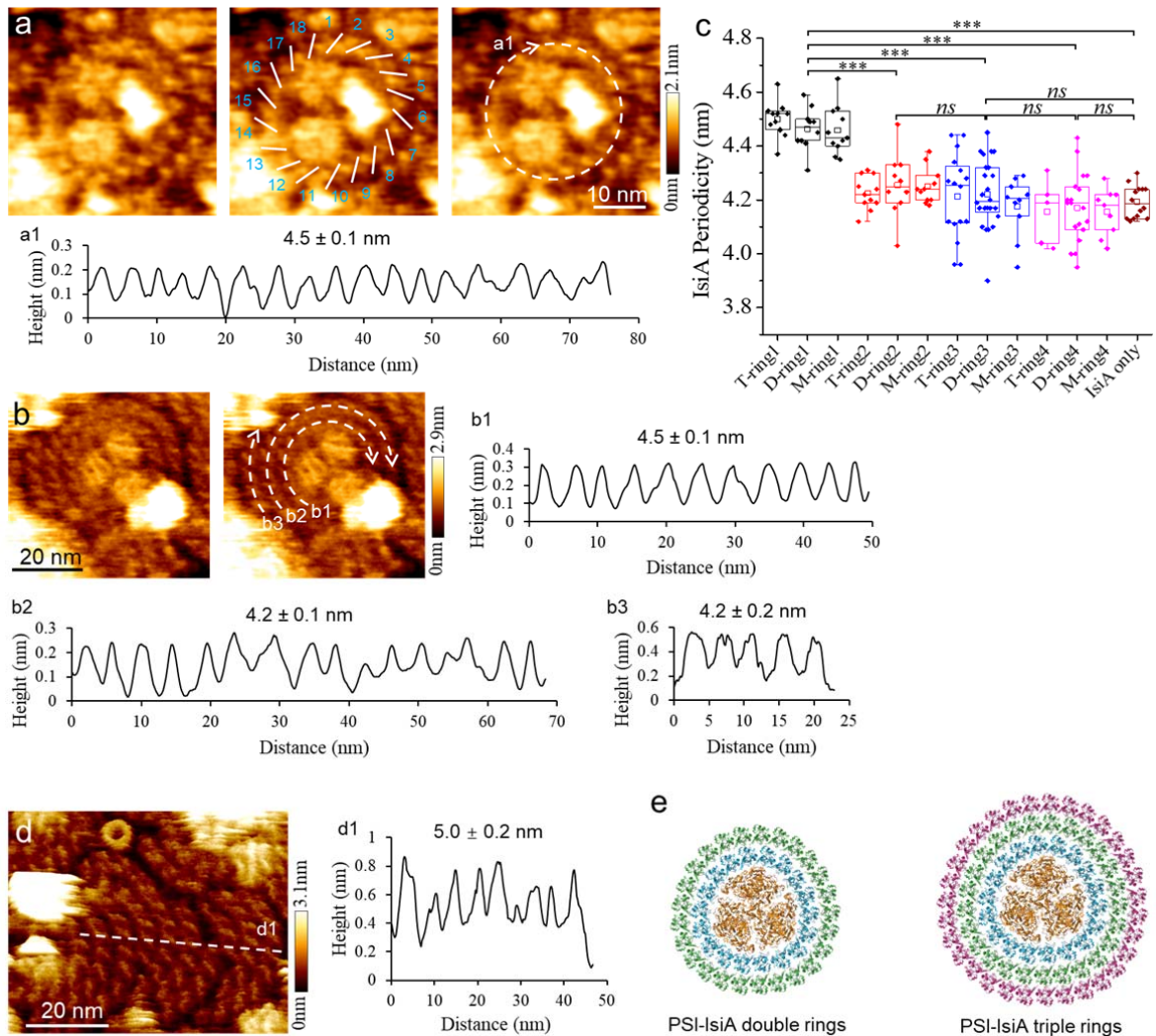
Fig. 4. Analysis of the IsiA organisation. a, Zoom-in view of an IsiA−PSI supercomplex which the first IsiA ring is intact. The spaces between the IsiA monomers are indicated by white bars, and eighteen IsiA subunits are identified. Height profile a1 is corresponding to the dashed circle. The periodicity of IsiA in IsiA rings is 4.5 ± 0.1 nm ($n = 160$ calculated distances between adjacent IsiA subunits). **b**, Zoom-in view of an IsiA−PSI supercomplex with three incomplete IsiA rings. Height profile b1, b2, b3 are corresponding to the dashed line b1, b2, b3. The periodicity of IsiA in the inner, middle and outer IsiA rings are 4.5 ± 0.1 nm ($n = 160$ calculated distances between adjacent IsiA subunits), 4.2 ± 0.1 nm ($n = 91$ calculated distances between adjacent IsiA subunits) and 4.2 ± 0.2 nm ($n = 17$ calculated distances between adjacent IsiA subunits) respectively. **c**, Box plots of IsiA periodicities in IsiA rings around PSI trimer (T), dimer (D), and monomer (M) and in IsiA self-assemblies. The numbers represent the position of a ring counting from PSI. Box plots display the median (line), the average (open square), the interquartile range (box) and the whiskers (extending 1.5 times the interquartile range). The number of calculated distances between adjacent IsiA subunits for each ring type (from left to right) is 160, 92, 73, 91, 98, 101, 17, 24, 62, 5, 19, 55, and 104, respectively. Statistical analysis was performed using two-sided two-sample t-Test, *** $p < 0.001$ (from left to right, $p = 6.51 \times 10^{-17}$, 2.68×10^{-15}, 4.75×10^{-19}, 2.20×10^{-15}, respectively), ns (no significance), $p_{(ring\ 2\text{-}3)} = 0.07$, $p_{(ring\ 3\text{-}4)} = 0.32$, $p_{(ring\ 4\text{-}IsiA\ only)} = 0.39$, $p_{(ring\ 3\text{-}IsiA\ only)} = 0.93$. **d**, Zoom-in view of IsiA self-assembly (3D enhanced) showing the IsiA fibres in more detail. Height profile d1 is corresponding to the dashed line d1. The periodicity of IsiA fibres is 5.0 ± 0.2 nm ($n = 18$ calculated distances between adjacent IsiA fibres). **e**, Structural models of the IsiA−PSI supercomplexes with double rings and triple rings constructed based on the cryo-EM structure (PDB: 6NWA) and AFM periodicity analysis. The representative AFM imaging was shown from at least five biologically independent membrane preparations.

885
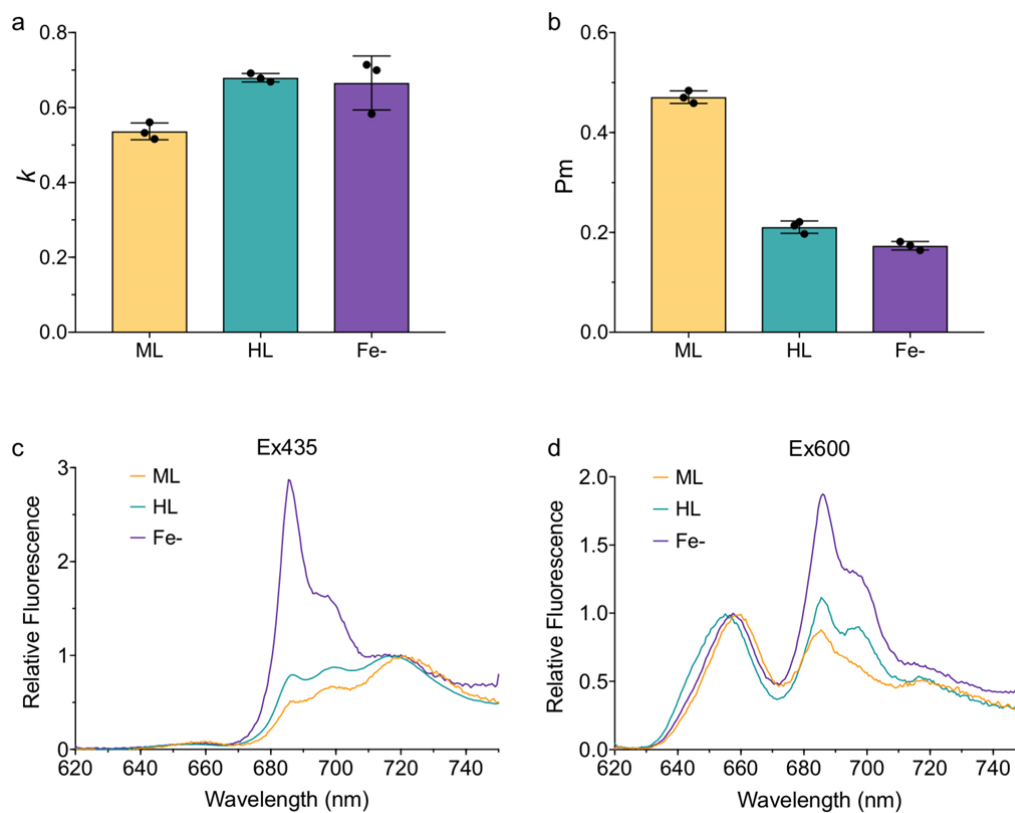
Fig. 5. Functional characterisation of IsiA in Syn7942 cells under ML, HL and Fe- conditions. a, k-values of 1st-degree exponential function fitted to the P700 oxidation kinetics after 620 nm saturating pulse (3 ms, 20 mmol photons·m^{-2}·s^{-1}). Samples were dark acclimated before each measurement and the Chl a concentration was adjusted to 20 μg·mL^{-1}. Values represent mean ± SD, n = 3 biologically independent experiments. **b**, The maximal amount of oxidised P700 (P$_m$) indicating the functionality of PSI. Values represent mean ± SD, n = 3 biologically independent experiments. **c**, Average 77K fluorescence emission spectra of cells with 435 nm excitation, n = 5 biologically independent experiments. **d**, Average 77K fluorescence emission spectra of cells with 600 nm excitation, n = 5 biologically independent experiments. In **c,** and **d,** Chl a concentration was adjusted to 10 μg·mL^{-1} for measurements.
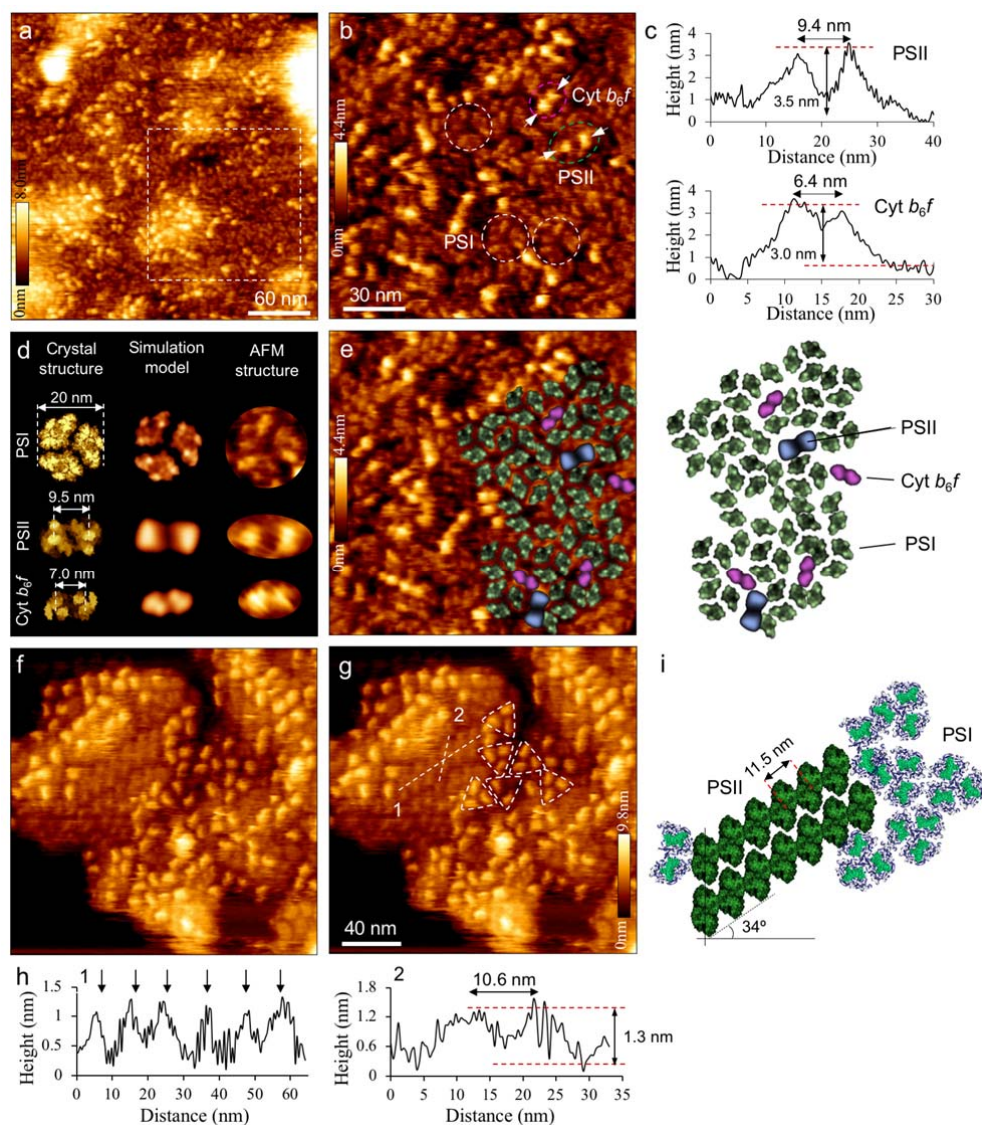
Fig. 6. AFM images revealing PSII and Cyt b_6f in the thylakoid membranes from ML-adapted Syn7942. a, High-resolution AFM image of the luminal surface of thylakoid membranes showing the densely packed photosynthetic membrane proteins. The area represented by the white box is shown in **b**. **b**, Zoon-in view of the area highlighted in **a**. PSI trimers are highlighted with white circle based on their unique topograph as shown in **d**. Putative PSII and Cyt b_6f complexes are highlighted with green oval and pink oval respectively, based on the space between their two monomers from the luminal membrane surface. White arrows show the positions of height profiles. **c**, Height profiles corresponding to the PSII and Cyt b_6f in **b**. The lateral distance between peaks of PSII is (8.9 ± 0.9 nm, $n = 15$) and the height of protrusions from the membrane surface is 3.5 nm. The lateral distance between peaks of Cyt b_6f is (6.2 ± 0.7 nm, $n = 15$) and the height of protrusions from the membrane surface is 3.0 nm. **d**, Atomic structure (left), simulated AFM images based on PDB (middle) and AFM topograph (right) of PSI, PSII and Cyt b_6f from the luminal surface (PDB, PSI: 1JB0, PSII: 3WU2, Cyt b_6f: 2E74). The lateral size of PSI crystal structure and distance of protrusions in the PSII and Cyt b_6f crystal structures are shown. **e**, Model of the arrangement of PSI, PSII and Cyt b_6f within the thylakoid membrane constructed with simulated AFM images of PSI (green), PSII (blue) and Cyt b_6f (purple). **f**, High-resolution AFM image of the cytoplasmic surface of thylakoid membrane showing the ordered array of dimeric complexes which are speculated to be PSII dimers. **g**, Same image as **f** with PSI trimers highlighted by triangles and positions of height profiles shown as dashed lines. **h**, Height profiles corresponding to the dashed lines in **g**. Black arrows show the peaks of profile 1. The lateral distance between peaks of profile 2 is 10.6 nm, and the height of protrusions from the membrane surface is 1.3 nm. **i**, Structural model of the arrangement of PSII dimers in ordered array and PSI trimers. The space between adjacent PSII dimer is 11.5 nm and the tilt angle of PSII array is 34°. The representative AFM imaging was shown from at least three biologically independent membrane preparations.
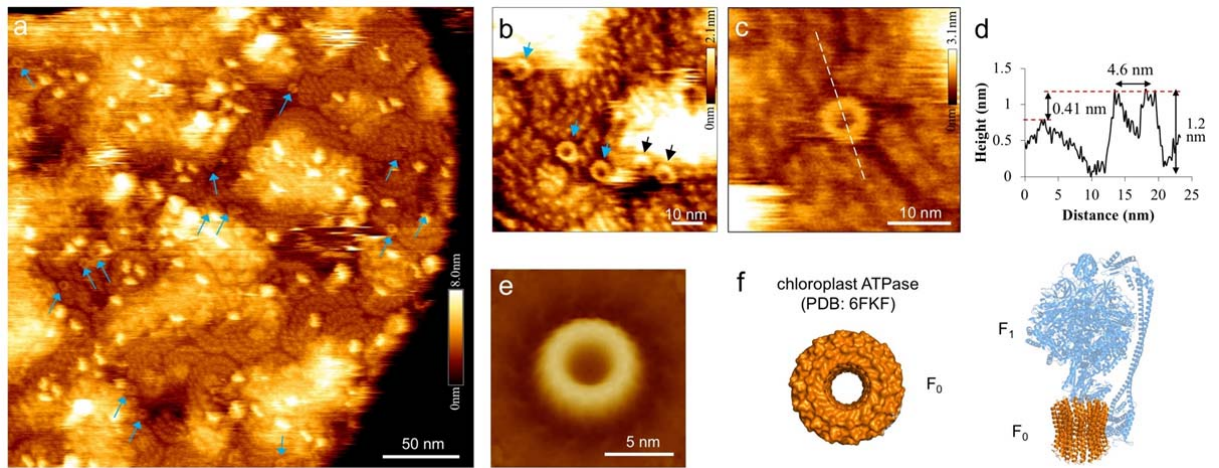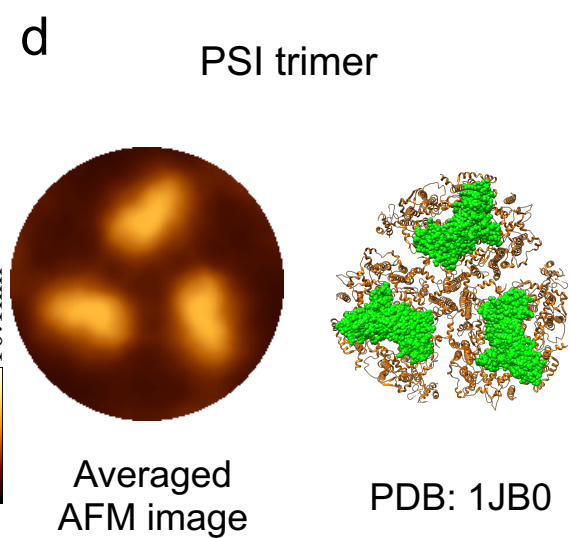
Fig. 7. AFM images of putative ATPases in thylakoid membranes. a, High-resolution AFM image of the cytoplasmic surface of thylakoid membranes. The speculated ATPase rings are indicated by blue arrows. **b**, High-resolution AFM image showing the rings more clearly. Blue arrows indicate the dispersive individual rings, and black arrows indicate the neighbouring rings. **c**, Zoom-in view to show the ring structure in more detail. Dashed line shows the position of height profile. **d**, Height profiles corresponding to the dashed lines in **c**, with lateral distances and height differences shown. **e**, The 14-fold symmetrised correlation average AFM topograph of the ring structure. **f**, Atomic structure of the chloroplast ATPase (PDB: 6FKF). Left panel shows the top view of membrane domain F_0. Right panel shows the front view of ATPase. The representative AFM imaging was shown from at least three biologically independent membrane preparations.
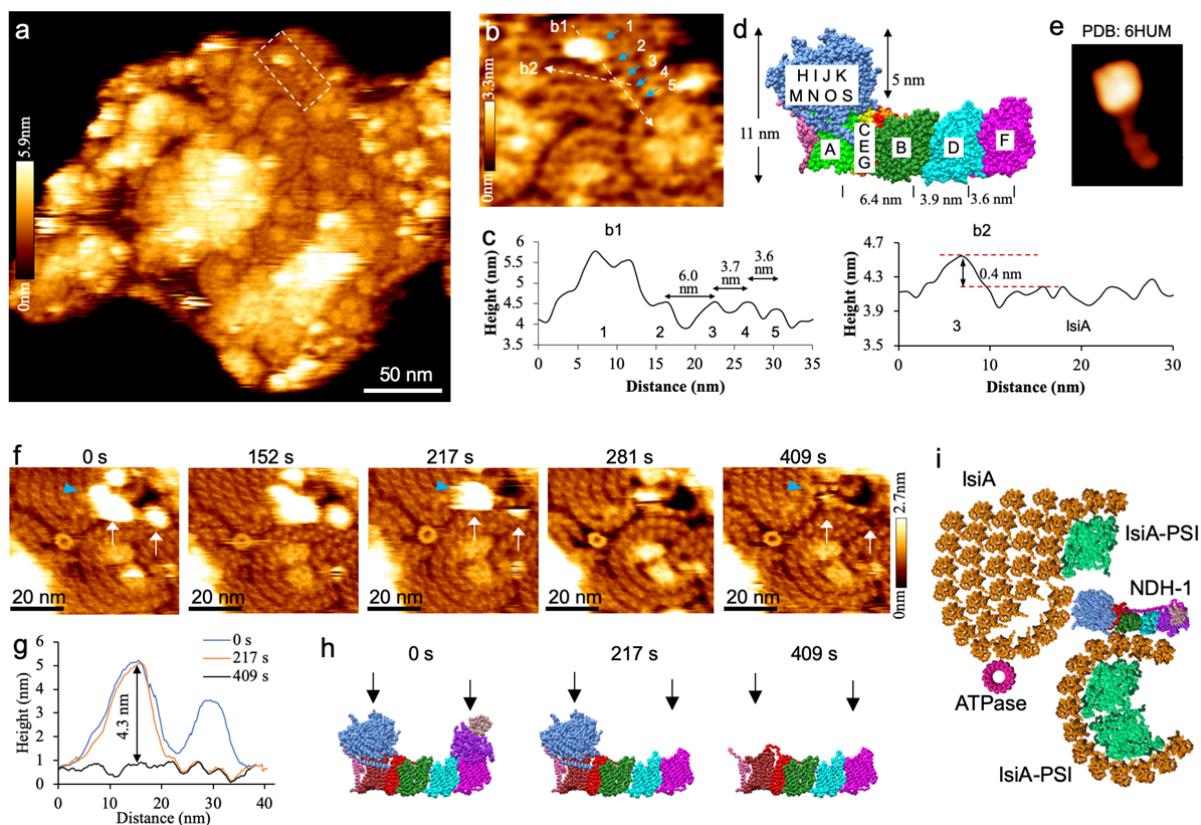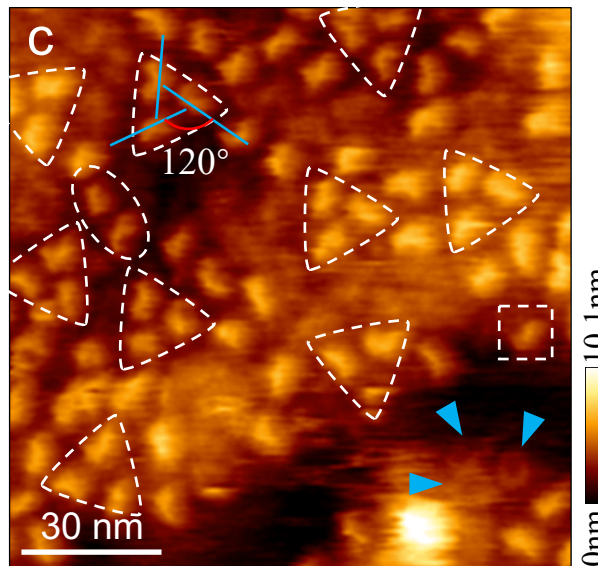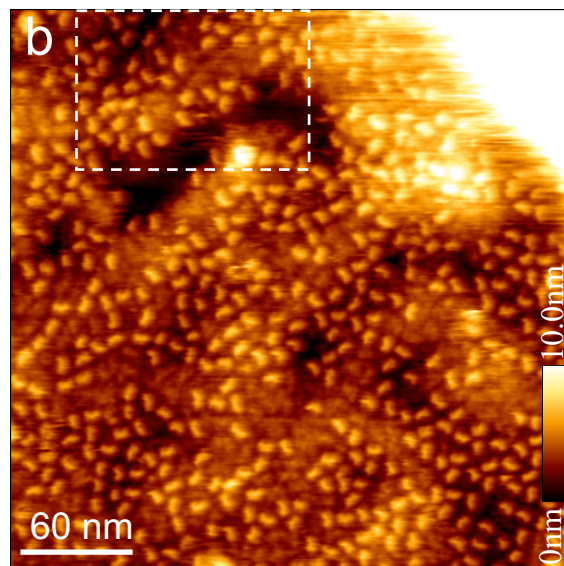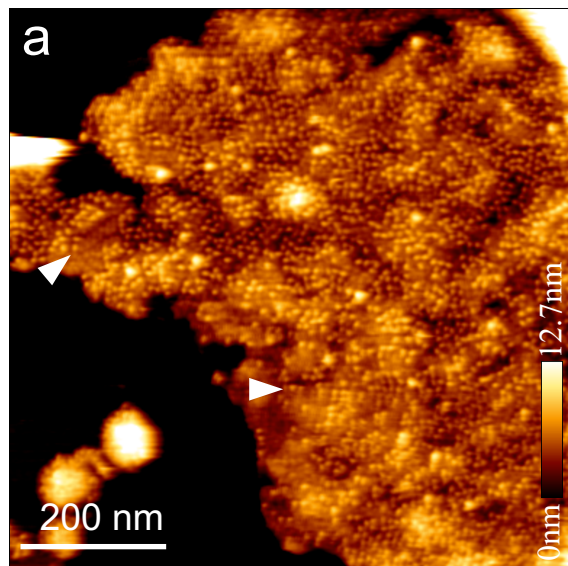
928
929 **Fig. 8. AFM images of putative NDH-1 in thylakoid membranes. a**, High-resolution AFM image of the
930 cytoplasmic surface of thylakoid membranes. The speculated NDH-1 complex is highlighted with white box.
931 **b**, Zoom-in view of the area highlighted in **a** showing the speculated NDH-1 complex in more detail. The
932 dashed lines show the positions of height profiles, and the blue arrows indicate the protrusions of NDH-1
933 complex. **c**, Height profiles corresponding to the dashed lines in **b**, with lateral distances and height
934 differences shown. **d**, Front view of the atomic structure of NDH-1 Complexes (PDB: 6HUM). The height is
935 11 nm, and the height above the membrane domain is 5 nm. The distances between the protrusions of four
936 membrane domains are 6.4 nm, 3.9 nm and 3.6 nm, respectively. **e**, Simulated AFM images based on the
937 cryo-EM structure (PDB: 6HUM). **f**, Time-lapse AFM imaging of NDH-1 complex, revealing the removal of
938 protruding subunits (white arrow). The blue arrow shows the position and direction of height profiles. **g**,
939 Height profiles of NDH-1 complex corresponding to the blue arrows in **f**. The height of the protrusion above
940 the membrane domain is 4.3 nm. **h**, Nanodissection of speculated NDH-1 complex in **f** is modelled with
941 NDH-1 atomic structure (PDB: 6TJV). Black arrows indicate the absent domains as shown in **f** with white
942 arrows. **i**, Structural model of the arrangement of IsiA−PSI, NDH-1 complex and ATPase. The representative
943 AFM imaging was shown from at least three biologically independent membrane preparations.

34

Moderate light (ML)

High light (HL)

a   0 s

10.3nm

0nm

50 nm

b   86 s

12.9nm

0nm

50 nm

c   c2   c1

d   d2   d1

e

10.1 nm

1.8 nm

c1

d1

Height (nm)

Distance (nm)

f

11.6 nm

1.8 nm

c2

d2

Height (nm)

Distance (nm)

g

20 nm

11 nm

2.6 nm

h

10 nm

i

Dissecting
PsaC
PsaD
PsaE

a AFM   Cryo-EM (PDB:6NWA)   Simulation

b Single ring   Double ring   Triple ring   Multiple ring

IsiA-PSI trimer

IsiA-PSI dimer

IsiA-PSI monomer

20 nm

c 30 nm

d 30 nm   25.7 nm

e 50 nm

f 50 nm   60.2 nm

a1 4.5 ± 0.1 nm

c

b1 4.5 ± 0.1 nm

b2 4.2 ± 0.1 nm

b3 4.2 ± 0.2 nm

d1 5.0 ± 0.2 nm

PSI-IsiA double rings

PSI-IsiA triple rings

a 8.0nm / 0nm / 60 nm

b 4.4nm / 0nm / 30 nm — Cyt b_6f, PSII, PSI

c
PSII: 9.4 nm, 3.5 nm — Height (nm) vs Distance (nm), 0–40
Cyt b_6f: 6.4 nm, 3.0 nm — Height (nm) vs Distance (nm), 0–30

d
Crystal structure / Simulation model / AFM structure
PSI — 20 nm
PSII — 9.5 nm
Cyt b_6f — 7.0 nm

e 4.4nm / 0nm — PSII, Cyt b_6f, PSI

f

g 4.0nm / 0nm / 40 nm — 1, 2, 9.8nm

i PSII, PSI — 11.5 nm, 34°

h
1: Height (nm) vs Distance (nm), 0–60
2: 10.6 nm, 1.3 nm — Height (nm) vs Distance (nm), 0–35

a

b

c

d

e

f chloroplast ATPase
(PDB: 6FKF)

F_0

F_1

F_0

a

b
b1
1
2
3
4
5
b2
3.3nm
0nm

c
b1
3.7 nm
3.6 nm
6.0 nm
1
2
3
4
5

b2
0.4 nm
3
IsiA

d
HIJK MNOS
5 nm
11 nm
A
C
E
G
B
D
F
6.4 nm
3.9 nm
3.6 nm

e
PDB: 6HUM

f
0 s
152 s
217 s
281 s
409 s
20 nm
20 nm
20 nm
20 nm
20 nm
2.7nm
0nm

g
0 s
217 s
409 s
4.3 nm

h
0 s
217 s
409 s

i
IsiA
IsiA-PSI
NDH-1
ATPase
IsiA-PSI